

## A Further Study of the Mechanisms of Cell Regeneration, Propagation, and Development within Two-Dimensional Multicell Storms

YUH-LANG LIN

*Department of Marine, Earth and Atmospheric Sciences, North Carolina State University, Raleigh, North Carolina*

LARA E. JOYCE

*DynTel Corporation, Research Triangle Park, North Carolina*

(Manuscript received 9 June 2000, in final form 16 March 2001)

### ABSTRACT

The mechanisms of cell regeneration, development, and propagation within a two-dimensional multicell storm proposed by Lin, Deal, and Kulie (hereafter LDK) were further investigated by conducting a series of sensitivity tests. LDK's advection mechanism was reexamined by performing simulations utilizing a plateau with five additional wind profiles having a wider range of shear. All five cases gave results that show that the cell regeneration period decreases with the storm-relative midlevel inflow, similar to that proposed by LDK. It was also found that a rigid lid is not an appropriate upper boundary condition for multicell storm simulations.

In order to test whether the advection mechanism is responsible for cell regeneration with a different sounding, an idealized sounding was used. A multicell storm was produced along with a strong density current and gust front updraft. Investigation of this storm supports the advection mechanism within the growing mode and a gravity wave mechanism in the propagation mode, as proposed by LDK. From further investigation, the relaxation mechanism proposed by Fovell and Tan was shown to exist within these simulations yet found to be dependent on the advection mechanism to cause cell regeneration.

To avoid some problems that occurred when using a plateau, a prescribed heat sink was used to produce a more realistic density current. This experiment demonstrates that the advection mechanism is responsible for cell regeneration and the gravity wave mechanism is responsible for cell propagation within the storm.

It was found that without precipitation loading, an individual cell is still able to split. In this case, the compensating downdraft produced by vertical differential advection is responsible for cell splitting and merging.

### 1. Introduction

In a recent study, Lin et al. (1998, hereafter LDK) proposed an *advection mechanism* for cell regeneration and a *gravity wave mechanism* for cell propagation within a multicell storm. The cell regeneration process is explained by the advection mechanism in LDK. They proposed that the following processes occur periodically during cell regeneration: (i) Near the edge of the gust front, the gust-front updraft (GFU) is formed by low-level convergence ahead of the gust front near the surface, (ii) the upper portion of the GFU grows by mid-level inflow since the gust front propagates faster than the basic wind, and (iii) the growing cell tends to produce, and is flanked by, strong compensating downdrafts. The upstream downdraft tends to cut off the growing cell from the gust front updraft. It was found

that the period of cell regeneration decreases as the mid-level, storm-relative wind speed increases.

In addition, LDK proposed that cell development and propagation within a two-dimensional multicell storm may be described in terms of two distinctive modes: (i) a growing mode, and (ii) a propagating mode. When a growing cell reaches its maximum intensity, it splits and then propagates downstream without amplification. The dynamics of cell development and propagation are explained by critical level arguments. For the growing mode, there is growth because of a conditionally unstable environment leading to steering level propagation, while for the propagating mode, there is no growth because of a more stable environment leading to propagation relative to the flow (i.e., absence of critical level). It was also found that the phase relationship between  $w'$  and  $\theta'$  ( $w'$  and  $u'$ ) in the growing mode is different from that in the propagating mode and can be explained by the dominance of latent heating in the thermodynamic equation. The propagating mode is dominated by horizontal advection. The propagating mode exhibits gravity wave properties, and propagates

---

*Corresponding author address:* Dr. Yuh-Lang Lin, Department of Marine, Earth and Atmospheric Sciences, Box 8208, North Carolina State University, Raleigh, NC 27695-8208.  
E-mail: yl.lin@ncsu.edu

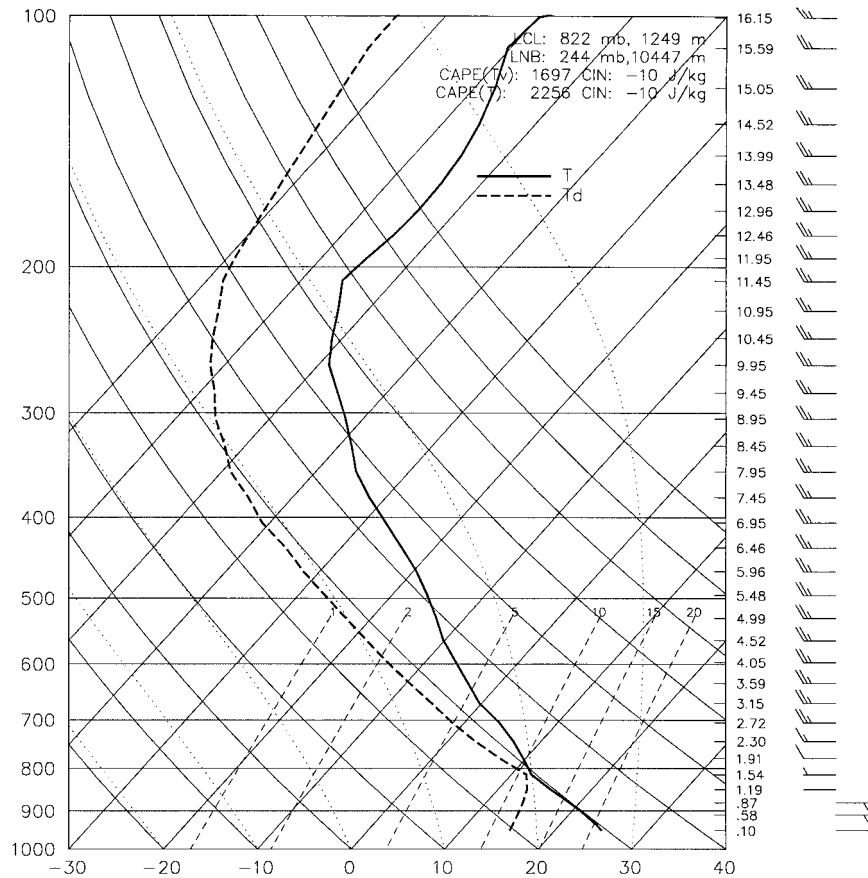


FIG. 1. Thermodynamic sounding from Fovell and Ogura (1988).

faster than the growing mode, which is consistent with the study of Yang and Houze (1995, hereafter YH).

In a recent study by Fovell and Tan (1998; hereafter FT98), they proposed that the cell life cycle could be divided into three stages: initiation, maturation, and dissipation. During stage 1, the buoyancy-induced circulation helps new cells rise and strengthen. The potentially warm air is ingested from below and the rising cell establishes a ribbon of potentially warm air in front-to-rear airflow emanating from low-level storm inflow. During stage 2, a growing cell's buoyancy-induced circulation acts to weaken forced lifting, reducing the potentially warm inflow. Concurrently, the stable, potentially cold air mixes into a cell's inflow wake from beneath, eroding its convective instability. On the rear-facing flank, the subsidence helps cut the new cell off from the previously generated cell. During stage 3, a cell's buoyancy-induced circulation on the front-facing flank weakens as mixing erodes instability. Then, the cell splinters and disorganizes. During the disorganization, the original, least diluted air effectively detrains from the splintered updraft, spreading out of the updraft (see Fig. 16 in FT98). Further mixing will completely erode the convective instability in its neighborhood. FT98 also proposed two advective timescales, which

control the timescale of cell regeneration. The first advective timescale is related to the movement of the previous cell's circulation, and the second one is based on the spatial extent of the "convective trigger" and the speed of the flow in which it is embedded. Basically, FT98's work is not inconsistent with LDK. Their three stages in the cell life cycle correspond to LDK's cell regeneration, growing mode, and propagating mode, respectively. Instead of cutting off from the old cell by the new cell on the rear flank as proposed by FT98, LDK proposed that the upstream (front-facing) downdraft associated with the growing cell cuts off from the gust front updraft in their advection mechanism. Our view is that this growing cell can be generated only after the old cell has propagated away from the gust front region, so that it is unlikely this growing cell will cut itself from the old cell as proposed by FT98. Regarding the timescale controlling the cell regeneration time, LDK has offered proof by adopting innovative plateau experiments. LDK found that the cell regeneration period decreases as the storm-relative midlevel inflow speed increases.

Although LDK's results provide strong arguments for each of their conclusions, further investigation is needed to evaluate the mechanisms for cell behavior within a

two-dimensional multicell storm due to the following reasons. One of the major concerns in LDK's simulations is that, in trying to prove the advection mechanism, they have replaced the cold pool with a plateau. Some potential problems may arise by using this approach (R.G. Fovell 1997, personal communication). (a) No mixing is permitted across the rigid obstacle boundary. The obstacle also precludes the development of Kelvin–Helmholtz waves along the cold outflow surface. (b) The real cold outflow has air moving within it. Owing to mass continuity, the presence of an impermeable obstacle can exert a substantial effect on the strength, orientation and character of the front-to-rear flow (FTR) occurring above it, including the path taken by parcels within this flow. (c) There is no baroclinically generated horizontal vorticity created at the obstacle nose, and apparently nothing to replace it or act in its stead. This could be a crucial component in the storm circulation, according to Rotunno et al. (1988). Although these deficiencies do not necessarily preclude the use of a rigid obstacle as a cold outflow proxy, it is important to reexamine LDK's advection mechanism by taking a more realistic approach. In this study, we plan to generate a cold outflow more naturally by prescribing a heat sink, such as those used in Lin and Chun (1991), Lin et al. (1993), and Jin et al. (1996). By doing so, the above-mentioned problems will be avoided. In addition, rainwater was deactivated in LDK's plateau simulations, which allows some unnatural growth of the clouds. To avoid this problem, we allow the precipitation to occur in this study, but deactivate the evaporative cooling.

In proving the advection mechanism, LDK has used the temperature and dewpoint profiles of Ogura and Liou's squall line (1980) with five basic wind profiles. In order to make sure that the proposed mechanism is at work in different environments, we reexamine LDK's advection mechanism with a different sounding, along with a wider spectrum of basic wind profiles. A rigid lid has been adopted as the upper boundary condition in some multicell storm simulations (e.g., Fovell and Ogura 1989). Although the adoption of a rigid lid may not modify the basic dynamics of cell regeneration, development, and propagation within a multicell storm, it is still important to isolate the effects exerted by the rigid lid. In this study, we perform a sensitivity test to the upper boundary conditions to identify the similarities and differences between the simulated results. In modeling the multicell storms in LDK and the present study, we also found that the convective cells embedded within the multicell storm have encountered some interesting splitting and merging processes. Thus, we will also make some efforts to explain this phenomenon.

The model utilized for the two-dimensional simulations is described along with the initial model conditions in section 2. The results of sensitivity tests on the advection mechanism for cell regeneration are presented in section 3. The sensitivity tests include 1) numerical simulations, which use a plateau to mimic the density

current with a wide range of low-level shear values; 2) simulations using a variety of upper boundary conditions; and 3) use of a different multicell sounding to initialize the model. Section 4 is comprised of results from two-dimensional numerical simulations of multicell thunderstorms in which a density current is initiated using a localized heat sink. Four different shear profiles were employed in this experiment. Section 5 contains results from a study of the mechanisms that may cause cell splitting and merging within a multicell storm. Finally, conclusions and discussion are made in section 6.

## 2. Model description and initialization

As in LDK, the Advanced Regional Prediction System (ARPS) version 4.2.4 is utilized to perform the simulations in this study. The ARPS model has been briefly summarized in LDK and the details of the model may be found in Xue et al. (2000, 2001).

For all the simulations described in this study, certain input parameters remain the same and are specified within this section. Some parameters were varied with each simulation and are specified in later sections. For all the simulations presented, the model was run in two-dimensional mode. Fourth-order (second-order) finite differencing of the advection terms was utilized in the horizontal (vertical). Both Coriolis and surface drag were ignored since their effect on short-lived multicell storms is negligible. The lower boundary is rigid and free-slip. The sponge layer was created using a Rayleigh damping which has a coefficient prescribed by

$$\nu(z) = (\nu_t/2) \{1 - \cos[\pi(z - z_b)/(z_t - z_b)]\}, \quad (1)$$

where  $z_b$  and  $z_t$  are the heights of the bottom and top of the sponge layer, respectively, and  $\nu_t$  is the maximum Rayleigh friction coefficient. The following parameters were used:  $z_b = 22$  km,  $\nu_t = 0.01$  s<sup>-1</sup>, and  $z_t = 12$  km (except in section 3b). The inverse of  $\nu_t$  is 20 times the large time step (5 s), which is recommended by Xue et al. (2000, 2001). The small time step is 1 s. The domain is 500 km in the  $x$  direction (200 km for section 4a simulations) and 22 km in the  $z$  direction. The horizontal resolution is 1 km, while the vertical resolution varies from 200 m at the surface to 800 m at the domain top. Wave reflections from lateral boundaries were minimized by using a relatively larger horizontal domain and an Orlanski-type radiation boundary condition.

All simulations (except for those in section 3c) initialized ARPS with the temperature and moisture profiles used by Fovell and Ogura (1988) (see Fig. 1). The sounding is a smoothed version of the Hinton, Oklahoma 1430 CST 22 May 1976 sounding presented by Ogura and Liou (1980). The sounding was taken 6.5 h before the passage of the squall line. The convective available potential energy (CAPE) of the sounding is  $\sim 2500$  J kg<sup>-1</sup>, its lifting condensation level (LCL), level

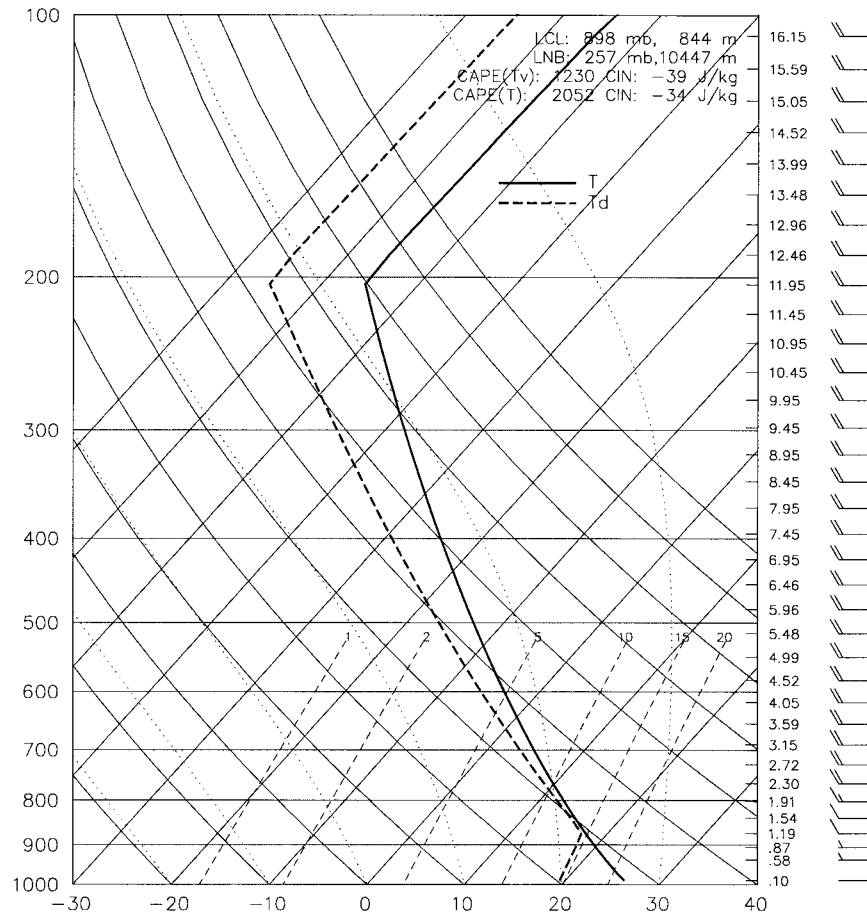


FIG. 2. Idealized thermodynamic sounding from Weisman and Klemp (1982).

of free convection, and level of neutral buoyancy are 1.8, 2, and 11.2 km, respectively. There is no convective inhibition. The vertical profiles of ground-relative wind vary for each simulation and are described in subsequent sections.

Simulations in section 3c were initialized with the idealized temperature and moisture profiles that were originally used by Weisman and Klemp (1982, hereafter WK82) to study the sensitivity to different environments. The vertical profiles of temperature and dewpoint are defined by analytic functions and are shown in Fig. 2. Some important features of this thermodynamic profile are a constant mixing ratio and a well-mixed boundary layer. A low LCL and a moist adiabatic parcel ascent depicted by a  $0.5^{\circ}$ – $3^{\circ}$ C negative buoyancy at the cloud base and a  $4^{\circ}$ – $10^{\circ}$ C of buoyancy at 500 mb is also noted. The relative humidity decreases steadily with the height above the mixed layer. No dry intrusion that is characteristic of some severe weather soundings is included. The calculated CAPE is  $2052 \text{ J kg}^{-1}$  and the convective inhibition (CIN) is  $-34 \text{ J kg}^{-1}$ , which are in the range for multicell convection.

### 3. Sensitivity to shear strength, upper boundary conditions, and soundings

#### a. Sensitivity to strong shear

A plateau was used by LDK to mimic the density current formed by a two-dimensional multicell storm in order to isolate the effects of basic wind advection on new cell generation without the complications of gust front oscillation. A westward basic wind was blown over the plateau to represent the relative wind with respect to the density current. The strong low-level wind encountering the stationary plateau created low-level convergence and therefore, strong forced positive vertical motion at the eastern edge of the plateau (similar to a gust front). Although this method was highly idealized, the process that took place when using the plateau was very similar to cell generation along an actual thunderstorm cold outflow without the disturbances of the initial storm. This experiment helped to support LDK's advection mechanism theory for multicell storm cell regeneration. However, only three different experiments with a small range of shear values were presented in their paper ( $\Delta U = 5, 7.5, \text{ and } 10 \text{ m s}^{-1}$ ;  $U_z = 2 \times 10^{-3}$ ,

### Wind Speed Profiles for Plateau Simulations

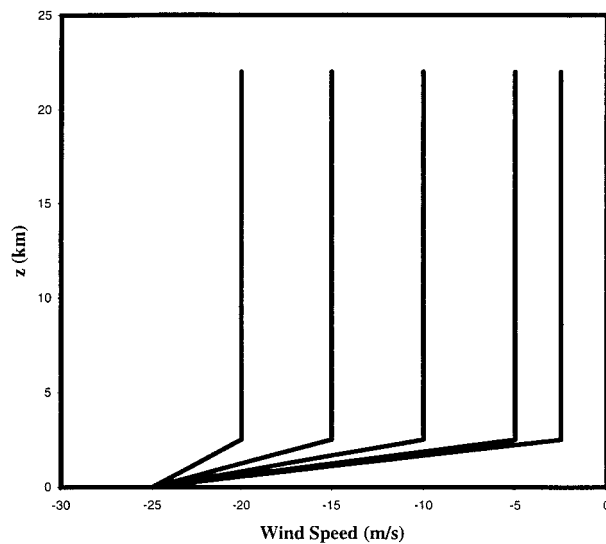


FIG. 3. Basic wind profiles utilized for the initialization of the plateau sensitivity test simulations.

$3 \times 10^{-3}$ , and  $4 \times 10^{-3} \text{ s}^{-1}$ ). Here, we will further investigate the sensitivity to shear strength.

In this study, five additional basic wind profiles with a much wider range of shear were utilized. The profiles (Fig. 3) have a uniform surface wind velocity of  $-25 \text{ m s}^{-1}$ , which increases to  $-20$ ,  $-15$ ,  $-10$ ,  $-5$ , and  $-2.5 \text{ m s}^{-1}$  at  $z = 2.5 \text{ km}$  ( $\Delta U = 5, 10, 15, 20$ , and  $22.5 \text{ m s}^{-1}$ ;  $U_z = 2 \times 10^{-3}, 4 \times 10^{-3}, 6 \times 10^{-3}, 8 \times 10^{-3}$ , and  $9 \times 10^{-3} \text{ s}^{-1}$ ) and is constant above this height. Precipitation (water loading) was also allowed in these plateau simulations unlike the nonprecipitating plateau experiments in LDK. This will avoid any unnatural growth of the simulated clouds.

The shape of the plateau was determined with the analytic function,

$$h(x) = \begin{cases} h_o, & \text{for } x \leq x_o, \\ h_o \cos[(\pi/2)(x - x_o)/a], & \text{for } x_o < x \leq x_o + a, \\ 0, & \text{for } x_o + a < x. \end{cases} \quad (2)$$

The following parameters were used for these simulations:  $h_o = 1.5 \text{ km}$ ,  $a = 6 \text{ km}$ , and  $x_o = 100 \text{ km}$ . The domain in the  $x$  direction in these simulations is only  $200 \text{ km}$  because the plateau is stationary and the additional lateral space in the computational domain for gust front movement was not needed.

Similar to LDK, convection was initially created by steady orographic forcing. Since the surface wind in all cases is  $-25 \text{ m s}^{-1}$ , it is similar to a case where the gust front is propagating at  $+25 \text{ m s}^{-1}$  and the surface winds are minimal. This approximately correlates with the speed of the gust front in the two-dimensional multicell sim-

ulation by LDK with  $\Delta U = 20 \text{ m s}^{-1}$  (see their Table 1). All five simulations were carried out at  $t = 2 \text{ h}$ .

The convective cells for all the cases simply became periodic by  $1 \text{ h}$  and remained organized throughout the simulation time. Figure 4 illustrates vertical velocity field cross sections for the case with  $\Delta U = 20 \text{ m s}^{-1}$  and a midlevel (above  $2.5 \text{ km}$ ) FTR inflow of  $5 \text{ m s}^{-1}$  from  $t = 60$  to  $104 \text{ min}$  with a time increment of  $4 \text{ min}$ . The topography  $h$  is illustrated by the solid, bold contour. This is an example of a highly sheared case. Figure 4 only displays the domain from  $x = 65$ – $130 \text{ km}$  in order to allow a closer look at the area of disturbance. The GFU is persistent and has a magnitude of  $\sim 7 \text{ m s}^{-1}$  up to a height of  $3.5$ – $4 \text{ km}$ . At certain times, however, the GFU is advected rearward by the midlevel FTR inflow. For instance, at  $t = 72 \text{ min}$ , the updraft (convective cell C1) has extended to a height of  $5 \text{ km}$  and is tilted slightly to the west. A gravity wave (G1) has also been generated above cell C1 by the GFU. By  $76 \text{ min}$ , cell C1 has tilted further rearward to  $x = 101 \text{ km}$  and a compensating downdraft (bold open arrow) to its right has developed that is separating the top of the tilted updraft from the GFU. Gravity wave G1 has propagated to the east during this time. By  $80 \text{ min}$ , C1 has grown vertically, has become completely independent from the gust front, and has shifted to the rear ( $x = 97 \text{ km}$ ). The GFU at this time has once again lowered to  $3.5 \text{ km}$  and G1 has begun to dissipate as it progresses forward. From Fig. 4, the rearward cell speed behind the gust front is estimated to be  $\sim 16.7 \text{ m s}^{-1}$ .

The updrafts (cells) are repeatedly generated, persist to the left, and continue to intensify while they propagate for a distance of  $\sim 20$ – $25 \text{ km}$ . Areas of strong subsidence divide the updraft cores. During the time period between cell initiation and its maximum intensity, the convective cell is in its growing mode (LDK). In Fig. 4, the growing mode occurs from  $x = 107 \text{ km}$  back to about  $x = 81 \text{ km}$ . During maximum updraft intensity, precipitation fallout to the surface ensues and subsequently, the cell dissipates (updraft strength weakens considerably) as it continues its rearward movement (Fig. 4;  $x < 81 \text{ km}$ ). Cell dissipation occurs because the liquid water drag weakens the updraft. Also, the supply of buoyant air east of the gust front to the location of the mature cell is inhibited due to the formation of new cells at the plateau edge (equivalent to gust front). During the time period after maximum updraft intensity, the convective cell is in its propagating mode (LDK).

The cells frequently split at the point of maximum strength as precipitation was initiated. This splitting process will be discussed in section 5. This cycle of GFU cell growth, detachment, and rearward movement was repetitious and continued throughout the entire simulation. Some weak gravity waves were generated by the GFU and move forward (to the right) although they quickly dissipate and do not produce any clouds or rain-water.

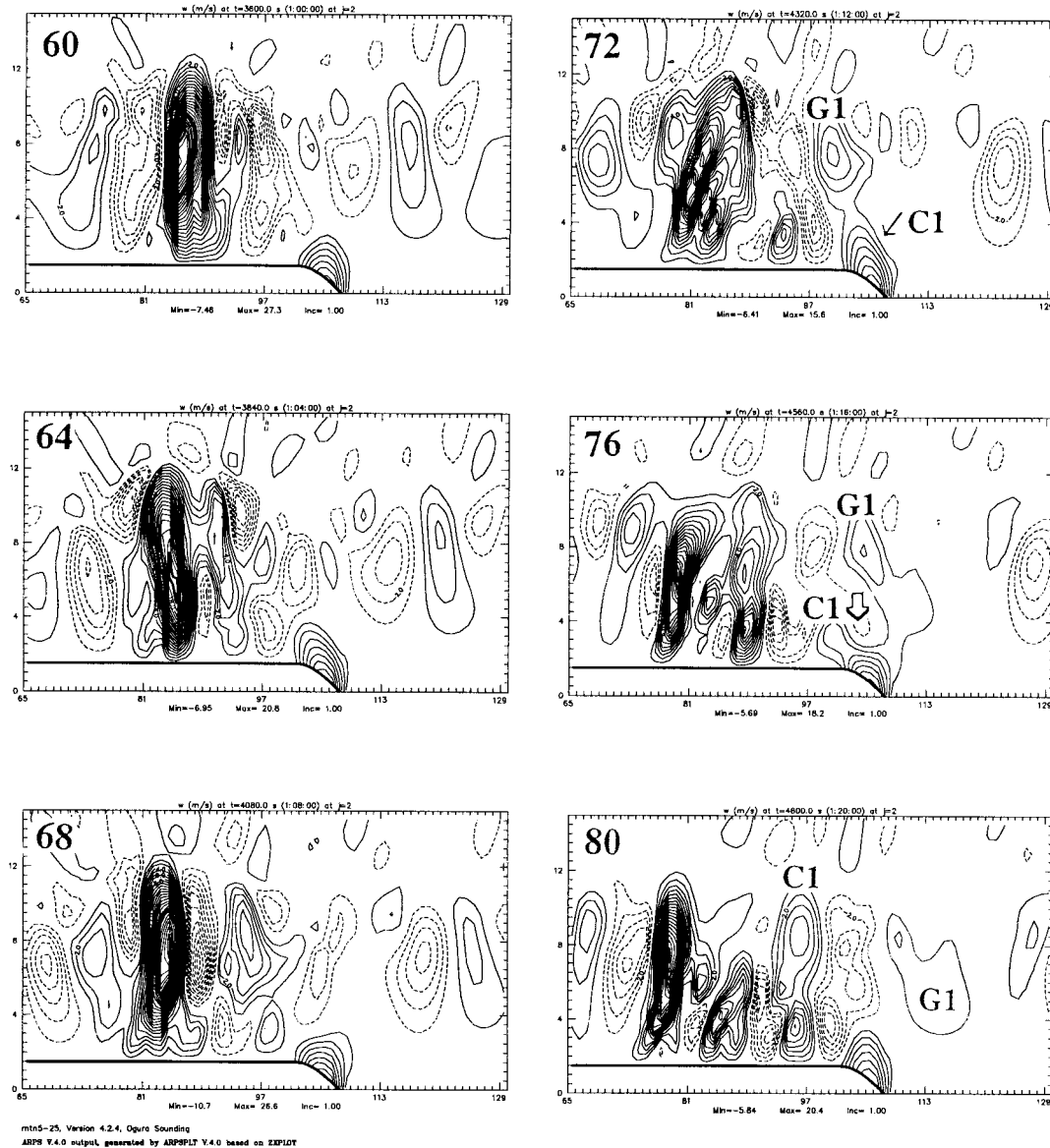


FIG. 4. Vertical cross sections of vertical velocity (contours in intervals of  $1 \text{ m s}^{-1}$ ) fields for an easterly flow over a plateau. The mountain height  $h_0$  and horizontal scale  $a$  used are 1.5 and 6 km, respectively. The basic wind profile has a uniform wind velocity of  $-5 \text{ m s}^{-1}$  above 2.5 km and increases linearly to  $-25 \text{ m s}^{-1}$  at the surface. The corresponding integration time (min) is shown in the left corner of each panel.

Time-space plots of vertical velocity and low-level rainwater mixing ratio are used to estimate the period of cell regeneration along the gust front. These periods were calculated and compared with the gust front-relative midlevel inflow velocities in order to verify LDK's advection mechanism. The cell regeneration period of 10.9 min determined from Fig. 5b is consistent with the cell regeneration shown along the plateau edge in Fig. 4. The phase speed of the cells can also be determined using time-space plots by observing the slopes of the phase lines connecting updraft maxima and minima.

Figure 5 shows the time-space plots of  $w'$  at a height of  $z = 2.7 \text{ km}$  for all five shear cases with plateau

employed. The midlevel inflow in this case is  $-5 \text{ m s}^{-1}$ . The midlevel inflow in cases with stronger shear (e.g.,  $\Delta U = 22.5$  and  $20 \text{ m s}^{-1}$ ) is extremely weak. Therefore, the steep slopes of the phase lines illustrate slow overall rearward movement of the cells. In contrast, the more horizontal phase lines of the weaker shear cases (Figs. 5c–e) indicate faster rearward cell propagation. The rearward cell speed during the growing mode of  $16.7 \text{ m s}^{-1}$  that was calculated from Fig. 4 is verified from Fig. 5b. The cells move west about  $x = 10 \text{ km}$  for every 10 min in this figure. Note that weak shear here means the plateau would be like a rapidly moving gust front that is difficult to be maintained by

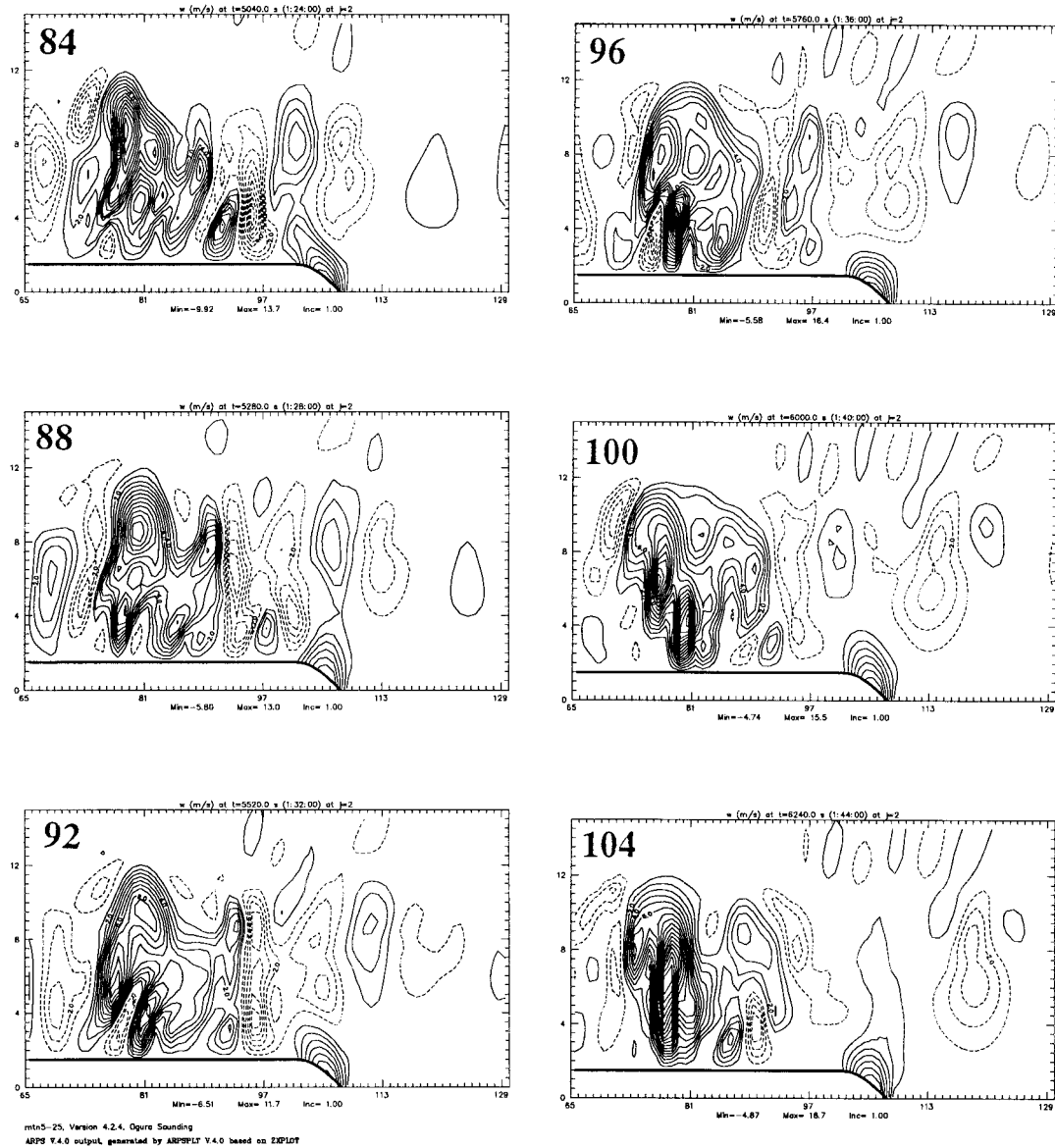


FIG. 4. (Continued)

precipitation evaporation, and so difficult to exist unless there is an external source of cold air.

From further analysis of the time-space plots of  $w'$ , we find that the weaker the wind shear, the stronger the midlevel inflow and the more discrete the cell generation. On the other hand, the stronger the wind shear, the weaker the gust front–relative midlevel inflow, and the more attached the generated cells are initially to the GFU. These findings are consistent with those of FO89 and Fovell and Dailey (1995). The cells in the low shear case form in a more discrete or independent manner similar to the strong evolution type of multicell storm (Foote and Frank 1983). The highly sheared case is more similar to that of the weak evolution multicell.

As pointed out by LDK, cells began to propagate rearward more quickly after they reached their maximum intensity and began to weaken (propagation mode). This notable difference in rearward cell speed can also be detected in YH's simulations and in Chalon et al.'s (1976) observation. The distinction in phase speed is clearly indicated by different angles of the constant phase angles (bold lines) in Figs. 5a–d. The cells grow and reach their maximum intensity by  $x = 81$ – $85$  km and move quite slowly ( $\sim 11.1$  m  $s^{-1}$ ). This growing mode is illustrated by steep phase lines. The mature cells then precipitate, lose intensity, and propagate more quickly ( $\sim 20.5$  m  $s^{-1}$ ) as they continue their rearward course ( $x < 81$  km). This propagating mode is depicted

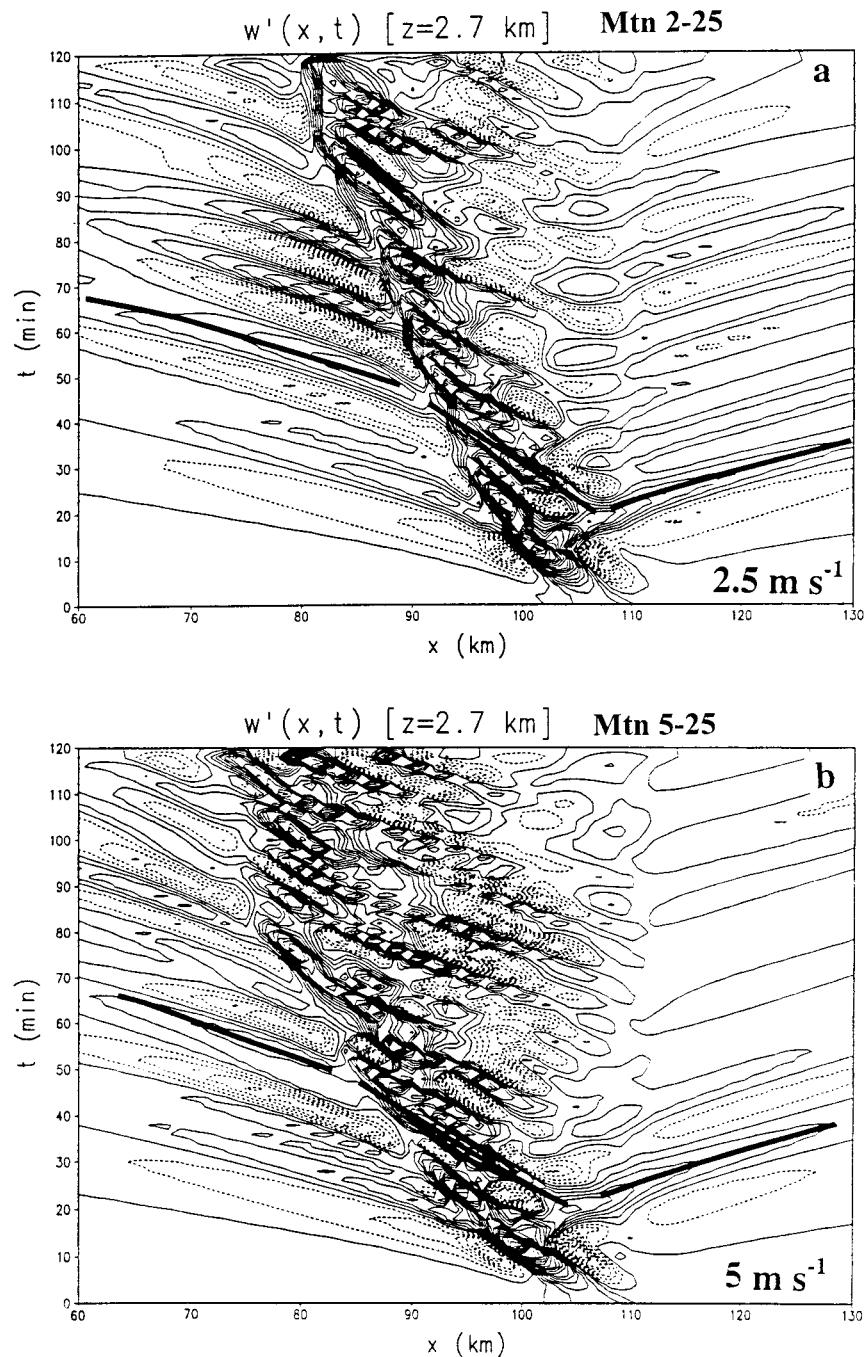


FIG. 5. Time-space plots of vertical velocity at  $z = 2.7$  km is given for all five easterly flows over plateau. The base-state wind speed above  $z = 2.5$  km is  $-5 \text{ m s}^{-1}$ . Positive (negative) values are solid (dashed). The storm-relative midlevel inflow is shown in the lower right corner. Heavy solid lines are representative of constant phase lines.

by the flatter phase lines. The phase lines for weak, forward-moving gravity waves ( $x > 107$  km) are also shown in Fig. 5.

LDK explained these two modes of rearward cell movement behind the gust front. The cells grow during the growing mode because they are within a condition-

ally unstable environment leading to steering (critical) level propagation. During the propagation mode, the cells are in a more stable environment and cannot develop further because of a lack of a steering level. Also, the stronger shear (weaker midlevel inflow) cases generate fewer cells along the GFU than the low shear cases

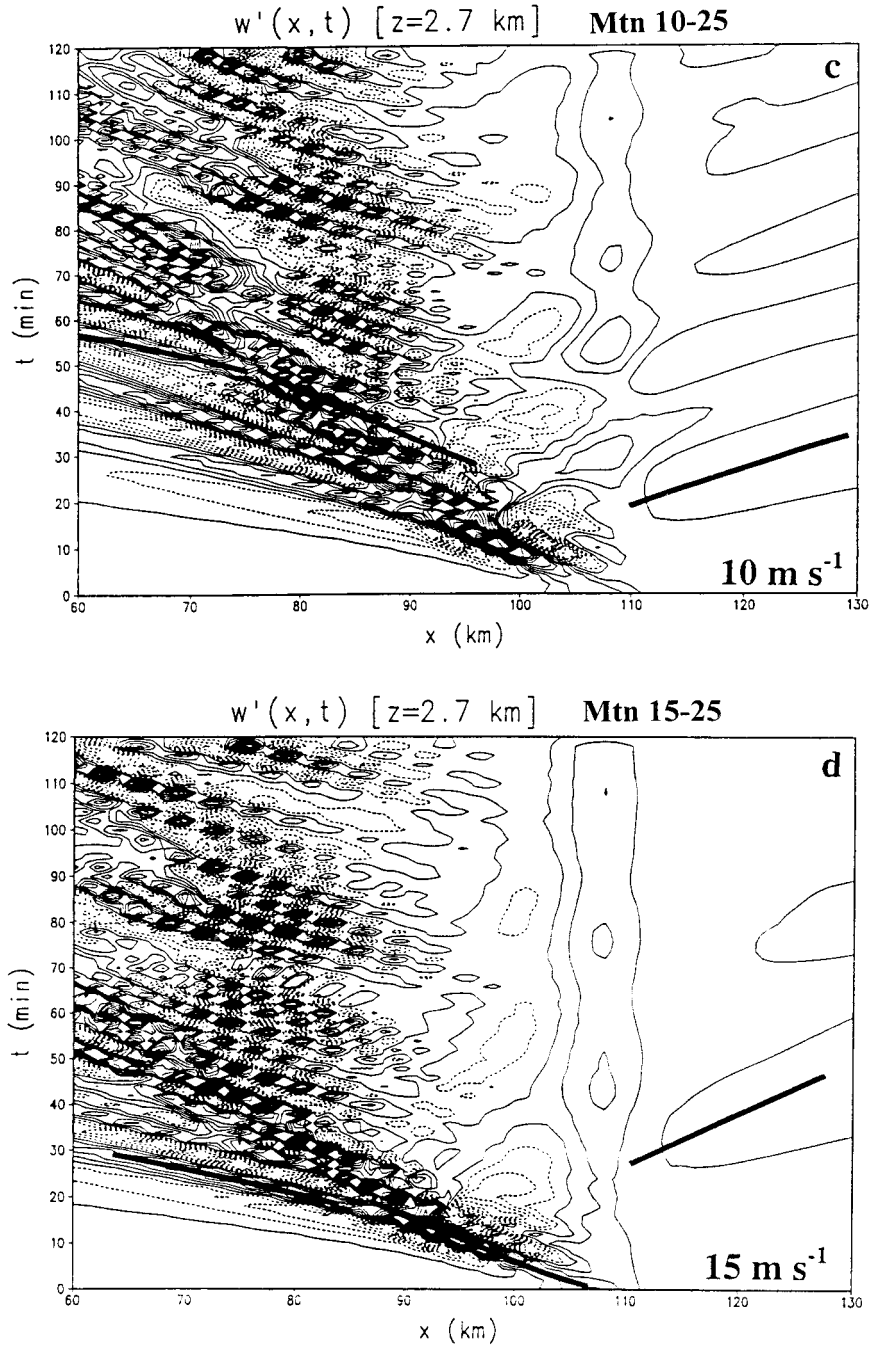


FIG. 5. (Continued)

within the same 120-min time period, as shown in Figs. 5a and 5b. Therefore, the cell regeneration period is larger. It should also be noted that from Figs. 5a and 5b it is apparent that the growing mode lasts longer (or extends farther rearward) as the simulation time increases. Although the cause of this extension of the growing mode with time is not verified, it may be due to the changing environment found behind the gust front. Initially, the conditionally unstable environment

needed for the growing mode was only found a certain distance ( $x \sim 16$  km) behind the gust front. However, with time the environment behind the gust front changes as cells propagate rearward. The conditionally unstable region behind the gust front extends farther to the west resulting in a longer growing mode.

As stated earlier, these plateau experiments also served to test the gust front oscillation mechanism (Thorpe and Miller 1978; Fovell and Tan 1996). This

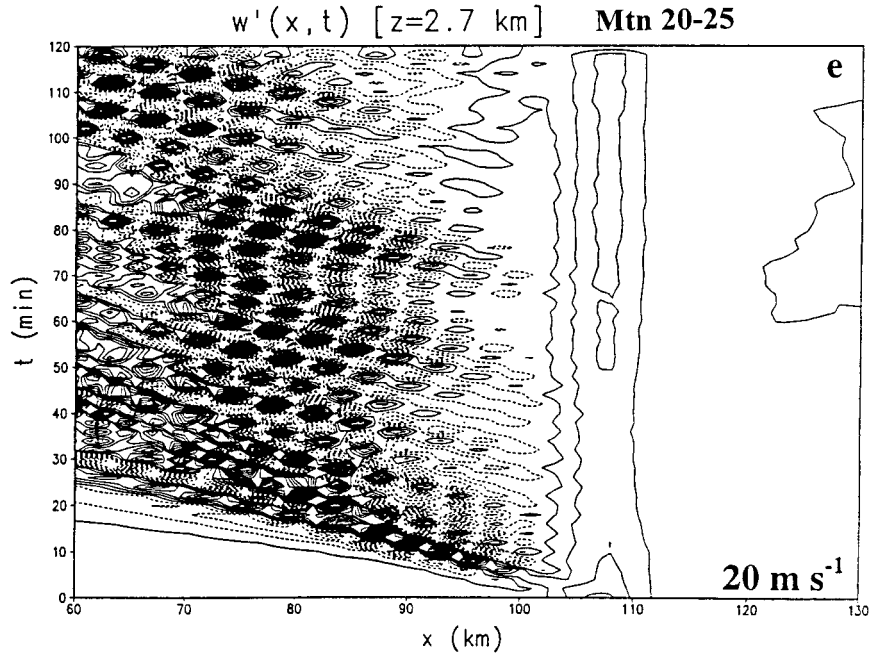


FIG. 5. (Continued)

hypothesis states that the spreading of the cold outflow of a mature cell accelerates the density current and enhances convergence; therefore, new cell generation at the gust front. However, the plateau experiment allowed no acceleration (or oscillation) of the gust front by keeping the plateau fixed. Periodic, discrete cell regeneration occurred in all five cases carried out by LDK, although there was no gust front oscillation. Therefore, this study suggests that the gust front oscillation mechanism is not necessary for cell regeneration within two-dimensional multicell thunderstorms. However, it is noted that water loading may have resulted in downdrafts that could have triggered new cell formation. The water loading issue will be addressed further in sections 4 and 5.

Table 1 gives a summary of the significant data from these experiments such as low-level ( $z < 2.5$  km) basic wind shear ( $\Delta U$ ); the surface wind speed that opposes the plateau ( $C_{dc}$ ), similar to gust front speed; storm-relative midlevel (3 km) inflow far ahead of the plateau edge (SRMLI); period of cell regeneration; and the

phase speed of growing-mode cell propagation. As the magnitude of the midlevel inflow increases, the cell regeneration period decreases and the propagation speed of the growing-mode cells increases. It is also noted that the magnitude of the low-level shear is directly related to the period of cell regeneration. Figure 6 depicts the relationship between midlevel inflow and the cell regeneration period for all the plateau cases. The relationship between the midlevel inflow and cell generation

TABLE 1. Sensitivity to stronger shear (section 3a).

$\Delta U$ ( $m\ s^{-1}$ )	$C_{dc}$ ( $m\ s^{-1}$ )	SRMLI ( $m\ s^{-1}$ )	Period of cell regeneration (min)	Propagation speed growing-mode cell ( $m\ s^{-1}$ leftward)
5	25	-20	5.45	29.9
10	25	-15	6.00	25.0
15	25	-10	7.06	21.4
20	25	-5	10.9	12.0
22.5	25	-2.5	13.3	11.1

PERIOD vs SRMLI: Plateau Simulations

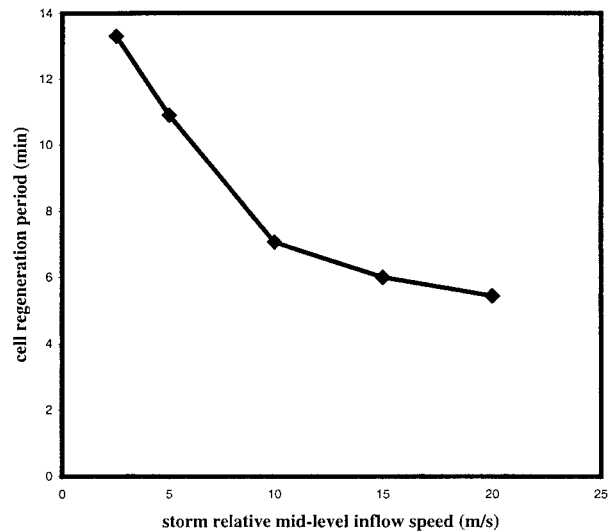


FIG. 6. Cell regeneration period vs the storm-relative midlevel inflow speed for flow over a plateau simulations.

period along the GFU is visibly apparent in this figure. From Fig. 6 it is also clear that as the SRMLI approaches zero, the cell regeneration period goes to infinity and no cells will be able to form. These discoveries from the plateau cases with a wider range of shear strengthen the evidence to support the advection mechanism proposed by LDK as one possible explanation for cell regeneration.

#### *b. Sensitivity to upper boundary conditions*

In previous multicell storm simulations, several different top boundary conditions have been utilized. For example, LDK utilized a sponge layer to mimic the upper radiation condition for allowing the energy associated with disturbances generated within the computational domain to propagate out of the domain. The use of an absorbing (sponge) layer was first proposed by Klemp and Lilly (1978) in a simulation of flow over rough terrain. Several authors (e.g., FO89; YH), however, opted to use a rigid lid top boundary in their multicell storm simulations. Another way to mimic the radiation condition is to apply an analytical function in Fourier space at the upper boundary of the computational domain (see Pielke 1984, for a review). Although the numerical radiation upper boundary condition is a more elegant way to implement the physical radiation boundary condition, we found it is more sensitive to the domain height used. Details of discussions on upper boundary conditions may be found in some textbooks (e.g., Pielke 1984) and will not be repeated here.

The simulations of flow over plateau reported upon in section 3a used the sponge layer described in section 2, which was 12 km deep (or one-half the domain height). This sponge layer top boundary (which is identical to that used by LDK) was employed so that the plateau simulations with additional wind shear profiles would be consistent with the research accomplished by LDK. To test whether a different top boundary condition would create any reflection or restrict the storm in any unphysical manner, we use a rigid lid upper boundary with no sponge layer. The upper boundary sensitivity simulation utilized a rigid lid at a height of 22 km. The sounding was the same as in Fovell and Ogura (1988) and LDK. An initial warm bubble of 2 K, which has a radius of 5 km in the horizontal and 1 km in the vertical, was used to trigger convection; evaporative cooling is allowed, which spreads into a cold outflow along the surface (no plateau is used in this experiment). The wind profile for this storm consisted of winds that increase from calm at the surface to  $10 \text{ m s}^{-1}$  at  $z = 2.5 \text{ km}$  and are constant above this height. These conditions are identical to the  $\Delta U = 10 \text{ m s}^{-1}$  sponge layer simulation from LDK so that the results may be compared with Fig. 7 (same as LDK Fig. 2).

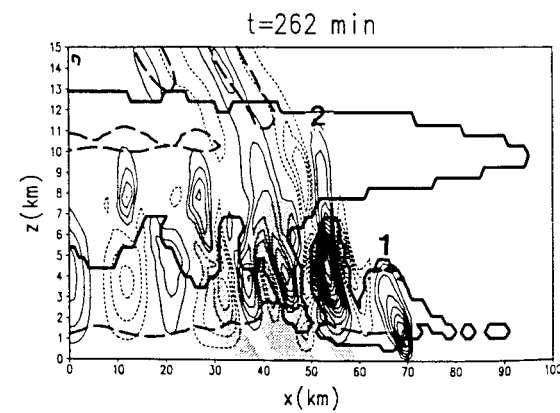
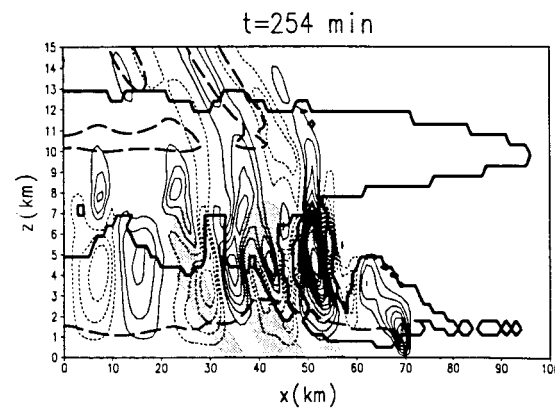
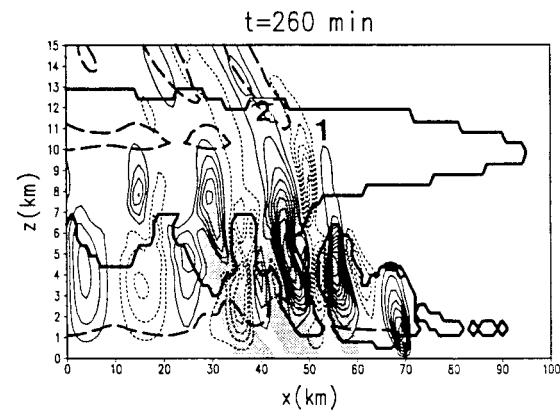
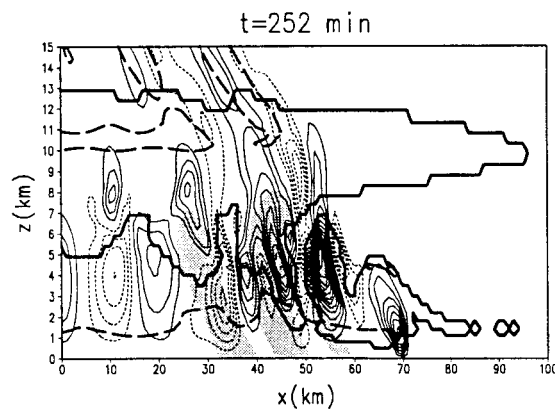
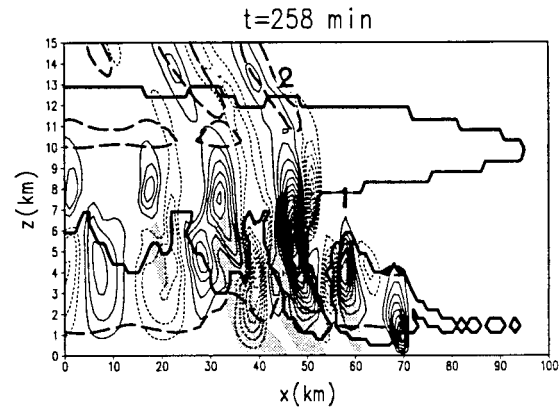
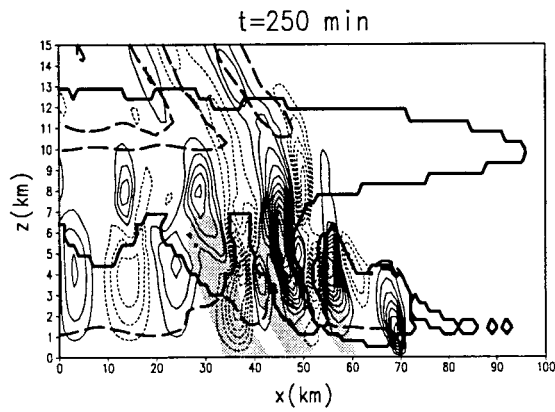
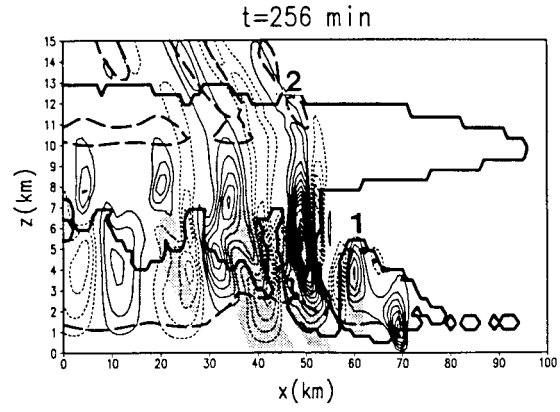
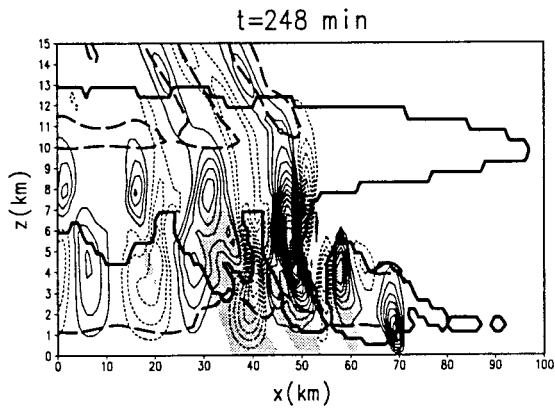
The results of the rigid lid simulation are shown in Figs. 8a and 8b, which display vertical cross sections of vertical velocity contours over the storm—induced

cold pool (density current) with rainwater shading from  $t = 248\text{--}262 \text{ min}$  (with 2-min increments). The vertical domain of the rigid lid simulation is the same as that of LDK; however, Fig. 7 only shows 15 km in the vertical. Figure 8a also exhibits the partial  $z = 15 \text{ km}$  height for comparison. The whole vertical domain ( $z = 22 \text{ km}$ ) in Fig. 8b is shown so that any reflections or disturbances by the rigid lid may be seen. The total horizontal domain in both simulations is  $x = 500 \text{ km}$  but both Figs. 7 and 8 show a smaller domain portion 100 km wide so that the disturbances may be more clearly illustrated. Both the simulations employed domain translation and therefore, the gust front is stationary in each figure at  $x = 70 \text{ km}$ .

A multicellular storm was produced with the rigid lid top boundary, similar to that with the sponge layer. Although the dynamical structures of the storms simulated by these two boundary conditions are similar, they do have some major differences. First, the general intensity of the storm generated in the rigid lid simulation (Fig. 8a) is much stronger than the storm in the sponge layer simulation (Fig. 7). The change in intensity is because the development of cells in these two simulations is very different. As stated previously, the growing mode is the time between when a cell is first generated at the GFU until the time when its updraft reaches its maximum magnitude (and has maximum precipitation fallout). In the sponge layer simulation, the growing mode is shown from  $x = 70 \text{ km}$  (GFU) to  $x \sim 50 \text{ km}$ . Within this area, two distinct cells are apparent, where the cell directly behind the GFU is rather weak and the second cell ( $x = 50 \text{ km}$ ) is the most intense.

In the rigid lid simulation, however, the growing mode is longer. The left panels of Fig. 8 show that the cells continue to grow from  $x = 70 \text{ km}$  to  $x \sim 40 \text{ km}$  (an additional 10 km). Also, there are three cells produced during the growing mode with the rigid lid as compared to two with the sponge layer. For comparison, the number of cells in the growing mode from  $t = 256\text{--}262 \text{ min}$  are labeled with numerals in both Fig. 7 and the left panels of Fig. 8. The two most mature updraft cores in this mode are stronger than the first growing updraft core (at  $x \sim 58 \text{ km}$ ); therefore, there are two cells within the growing mode with strong vertical motion compared to only one in the sponge layer case. More widespread areas of rainfall are also seen in the rigid lid simulation than those in the case with sponge layer, where the areas of surface precipitation are more distinct. This is due to the fact that the cells in the rigid lid simulation have a slower rearward propagation speed than the cells for the case with sponge layer. In addition, phase tilting in the upper levels ( $z > 10 \text{ km}$ ) is seen in the sponge layer case (Fig. 7) during the propagation mode. This represents upward-propagating gravity waves. However, the rigid lid case (Fig. 8) does not illustrate this phase tilting, which indicates trapped gravity wave structures.

The substantial reflection of energy from the rigid lid



top boundary is the cause of the unnatural strengthening of the storm simulation. For example, in the right panels of Fig. 8, the reflection of energy from the top boundary is clearly visible at the upper left corner of the figures. At  $x = 10$  km and  $z = 20$  km at each time shown, there is evidence of a disturbance being reflected down from the rigid top boundary ( $z = 22$  km). The significant differences between the rigid lid simulation and the storm simulated with the sponge layer are caused by the downward reflection of energy by the rigid lid upper boundary. This unphysical interference causes the simulated storm to be generally stronger, has a longer growing mode, and has slower cell rearward movement. Thus, a rigid lid is not an appropriate upper boundary condition to be used for multicell storm simulations.

### c. Sensitivity to soundings

Although the advection mechanism for cell regeneration and propagation has been well supported using both multicell storm simulations and the idealized plateau simulations, all of these experiments were initialized with the thermodynamic sounding used by Fovell and Ogura (1988). To test whether the advection mechanism is sensitive to thermodynamic profiles, an idealized sounding utilized by WK82 was adopted to initiate multicellular convection. The relaxation oscillation mechanism proposed by Fovell and Tan (1996) will also be examined. The details of the sounding are described in section 2. Three basic wind profiles (Fig. 9) were employed with low-level shear (below 2.5 km) values of  $\Delta U = 7.5, 10,$  and  $15 \text{ m s}^{-1}$ . Although this is not a wide range of shear, the values are representative of typical moderate multicell thunderstorm shear magnitudes (WK82) and the three simulation results obtained were sufficient to test the advection mechanism, as revealed by the LDK simulations. A  $\Delta U = 20 \text{ m s}^{-1}$  case was also performed; however, the shear was too strong for the storm to persist and it dissipated soon after the normal organization stage of 1 h.

An initial thermal bubble similar to that used in section 3b was utilized. Its center was placed 100 km from the western boundary and 1 km from the surface. Both precipitation and evaporative cooling were allowed to naturally create a realistic cold outflow. The domain grid was translated at the speed of the gust front and therefore, kept the area of disturbance stationary within the domain so it could be more easily analyzed. The storms needed about 1 h to organize and they all became fully periodic by 3 h. The simulations were carried out through  $t = 6$  h. All the storm simulations continued to exhibit organized, periodic cell production and prop-

agation through this time and showed no signs of dissipation.

By  $t = 30$  min in all cases, the thermally induced convection produced surface precipitation and a cold outflow began to propagate outward along the surface from the evaporative cooling. The depth of the outflow varied with each case but is on average from 1–3 km. The edge of the cold outflow spread in both horizontal directions, but substantial “semioptimal” convection was limited to the eastern (right) gust front where the positive vorticity found in the density current head opposed the negative vorticity caused by the basic wind shear (Rotunno 1988). The strong convergence at the gust front, which produced the forced lifting needed for convection, was formed because the cold outflow was moving more quickly than the basic wind speed. The western (left) side of the cold air only produced weak, slanted “suboptimal” convection, which quickly dissipates.

Figure 10 shows vertical cross sections of vertical velocity fields perpendicular to the eastern gust front over the cold outflow from  $t = 2$  h (7200 s) to  $t = 3$  h 15 min (11 700 s) (in 5-min time increments) for the  $\Delta U = 7.5 \text{ m s}^{-1}$  case. Rainwater mixing ratio greater than  $5 \times 10^{-4} \text{ g kg}^{-1}$  is shaded. This figure also indicates that the storm is indeed in an organized (quasi-steady) stage. The gust front is stationary at  $x = 167$  km in this figure, but without domain translation, the gust front propagation speed is estimated to be  $13.7 \text{ m s}^{-1}$ . As in the LDK simulations, the GFU intensified, grew vertically, and began to tilt rearward.

This cell initiation and tilting at the gust front is well illustrated at  $t = 8100$  s (see bold arrow). By  $t = 8400$  s, the eastern compensating downdraft (open arrow) of the growing cell has separated the top of the convective cell from the gust front. The cell begins to propagate rearward, and is shown at  $x = 155$  km. At  $t = 8700$  s, this cell has continued to grow to its maximum intensity and is located at  $x = 150$  km. Here, the cell unloads a large amount of surface precipitation. Behind  $x = 150$  km, the cells (updraft cores) dispose the remainder of their rainwater, begin to weaken, and move rearward at a more rapid pace (propagating mode). Another tilted cell has formed at the GFU and by  $t = 9000$  s, it too has been cut off from the GFU and has merged with the more matured cell. An in-depth discussion on the forcing mechanisms of cell splitting and merging is given in section 5. This process of gust front cell regeneration, splitting, and rearward propagation is periodic and is evident in all three shear cases (cases of  $\Delta U = 10$  and  $15 \text{ m s}^{-1}$  not shown).

The storm-relative midlevel ( $\sim 3$  km) inflow found

←

FIG. 7. Vertical profiles of vertical velocity (thin contours in intervals of  $1 \text{ m s}^{-1}$ ) for a portion of the domain in the moving frame of reference of the gust front for the  $\Delta U = 10 \text{ m s}^{-1}$  case with a sponge layer top boundary condition (from LDK).

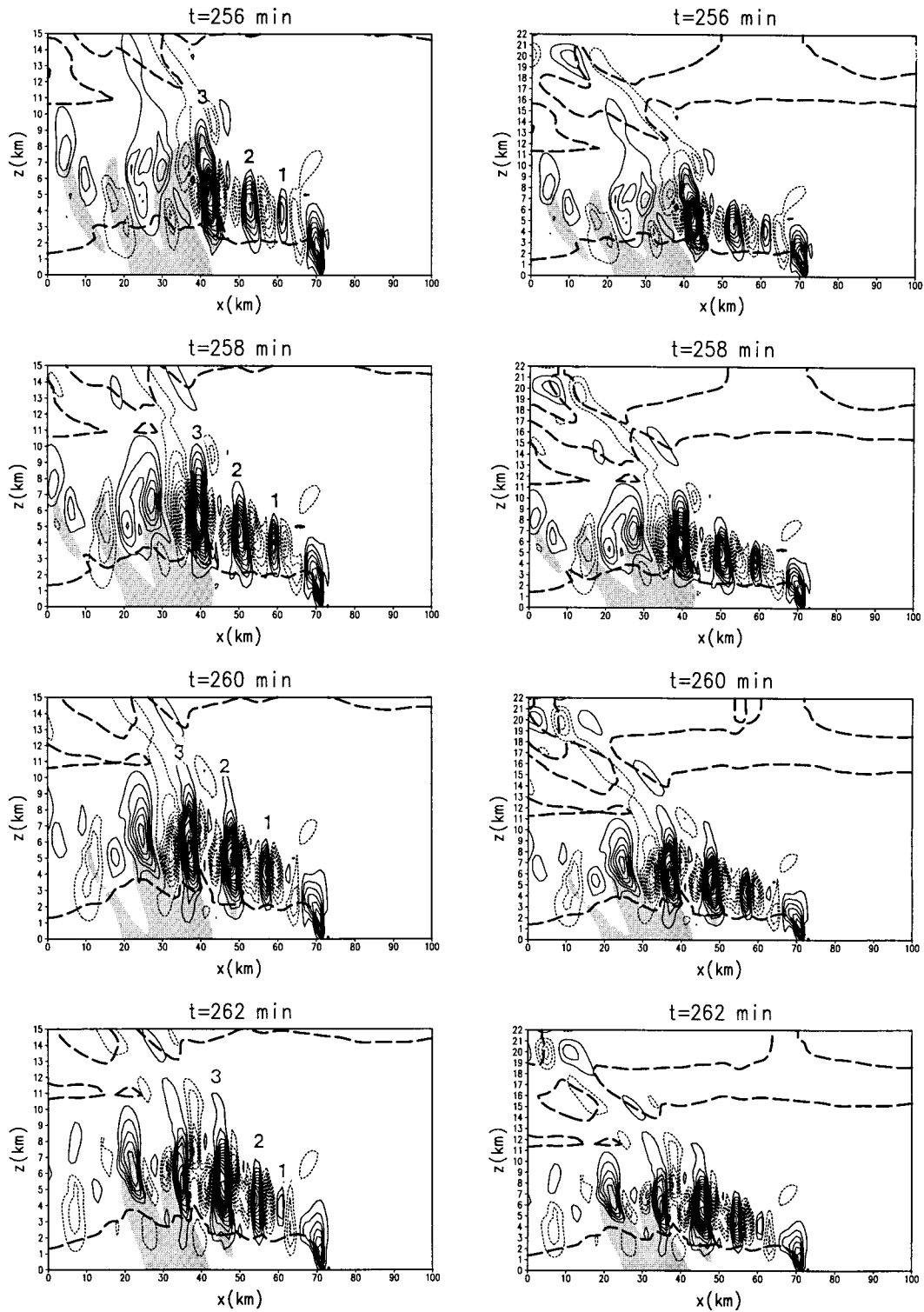


FIG. 8. As in Fig. 7 except for a rigid lid top boundary and for  $t = 256$ – $262$  min. Positive (negative) values are solid (dashed). The density current is represented by the  $-1$ -K potential temperature perturbation contour (bold dashed) near the surface. The rainwater is shaded ( $>0.0005 \text{ g kg}^{-1}$ ). The corresponding integration time is shown at the top of each panel. Results with partial vertical domain ( $z = 15$  km) are shown in the left panels, while those with total vertical domain ( $z = 22$  km) are shown in the right panels.

### Wind Speed Profiles for Idealized Sounding Multicell Simulations

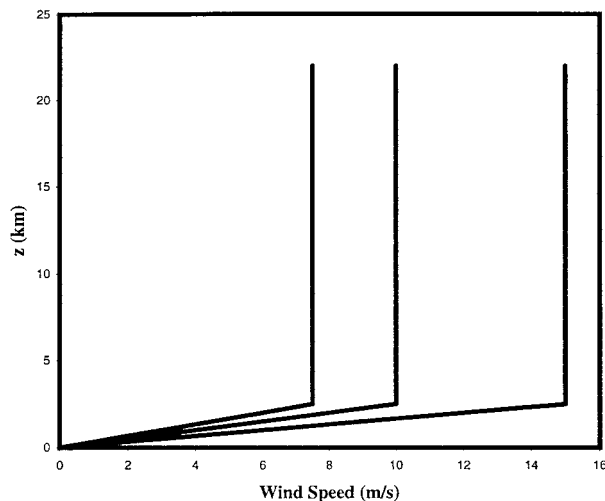


FIG. 9. Basic wind profiles utilized for the initialization of the Weisman and Klemp (1982) sounding multicell simulations.

well ahead of the gust front from the case of  $\Delta U = 7.5 \text{ m s}^{-1}$  is illustrated by the positive vertical velocity field (shaded) over the density current (denoted by bold line near the surface) in Fig. 11. Nearly conserved,  $\theta_e$  can be considered as a tracer except where mixing exists. Therefore, the statement by Fovell and Tan (1996) that the convective cells are moving in the FTR flow that originates in the low levels is only partially accurate. The cells are moving in a front-to-rear airflow, yet this air is primarily from mid levels. The quickly moving high  $\theta_e$  air originates in the low levels and is forced upward in the GFU to form new cells, but the cells are advected rearward by the slower midlevel inflow (see arrows Fig. 11,  $t = 8700 \text{ s}$ ).

The time–space plot of vertical velocity at  $z = 3 \text{ km}$  for the case of  $\Delta U = 7.5 \text{ m s}^{-1}$  is shown in Fig. 12. Figure 12 depicts the storm from  $t = 4$  to  $6 \text{ h}$  since it is most periodic during this time period. As in the plateau cases, this figure indicates that the cells originate at the gust front repeatedly and then move rearward with time. The distinct growing mode and the faster propagation mode that were described in the plateau experiment discussion are evident in these multicell time–space  $w'$  figures as well, although not as obviously. Results from cases of  $\Delta U = 10$  and  $15 \text{ m s}^{-1}$  (not shown) are similar to that of Fig. 12. From the  $w'$  field, it is apparent that as low-level wind shear increases (or midlevel inflow decreases), the cells generated at the gust front are less discrete. The individuality of the cells for each of these three cases is also apparent in Fig. 12. This result is consistent with the results from the LDK experiments.

The analysis of the phase relationships between  $p'$ ,  $u'$ ,  $\theta'$ , and  $w'$  within the storm simulated in this study

produced results similar to LDK, which is also similar to YH except for the phase relationship between  $\theta'$  and  $w'$ . Figures 13a, b, c illustrate the relationship between  $p'$ ,  $u'$ ,  $\theta'$ , and  $w'$  at  $t = 15\,300 \text{ s}$ . It is evident that from  $x = 162$  to  $140 \text{ km}$ , the  $\theta'$  maxima (Fig. 13c) are collocated with the updrafts throughout all levels, which is in contrast to the conclusions from YH. However, for  $x < 140$  the  $\theta'$  maxima are one-quarter wavelength behind the updrafts in all layers, which is consistent with YH. Therefore, the early and late stages of cell development have different phase relationships between  $\theta'$  and  $w'$ . The increase in cell speed between these growing and propagating modes (early and late stages) has already been demonstrated with Figs. 5 (plateau simulations) and 12 (idealized sounding simulations) and those in LDK. As originally proposed by LDK, these findings disprove the fact that gravity waves control the cells during the growing mode. However, gravity waves have been further proved as the controlling mechanism during the propagation stage, as proposed by LDK and YH.

A comparison of the gust front speeds ( $C_{dc}$ ), storm-relative midlevel inflow speeds (SRMLI), and cell regeneration periods for these three two-dimensional multicell storm simulations is summarized in Table 2. The low-level shear is again proportional to the period of cell regeneration. The calculated cell regeneration period along the gust front decreases as the storm-relative midlevel inflow increases in this experiment (Fig. 14). It is found that the advection of the top of the GFU by the storm-relative midlevel inflow (advection mechanism) is a necessary feature for cell production and movement (during the growing mode) within these simulated multicell storms that have a different environmental temperature and humidity profile.

## 4. Heat sink simulations

### a. Experimental design

Although the plateau employed to mimic the density current in LDK was an innovative way to isolate the complex characteristics of the density current, as mentioned in the introduction, it has raised some concerns. In order to avoid these problems, a heat sink was used in the model to produce a more realistic density current. The method of using a localized cold region to initialize a density current within a numerical model has been successfully used in several research projects such as Thorpe et al. (1982), Dudhia et al. (1987), Lin and Chun (1991), LDK, and Jin et al. (1996). The diabatic forcing, which represents the evaporative cooling of the falling precipitation, is given by

$$Q(x, z) = \begin{cases} Q_o \left[ \frac{a_1^2}{x^2 + a_1^2} - \frac{a_1 a_2}{x^2 + a_2^2} \right], & \text{for } 0 \leq z \leq d, \\ 0, & \text{elsewhere,} \end{cases} \quad (3)$$

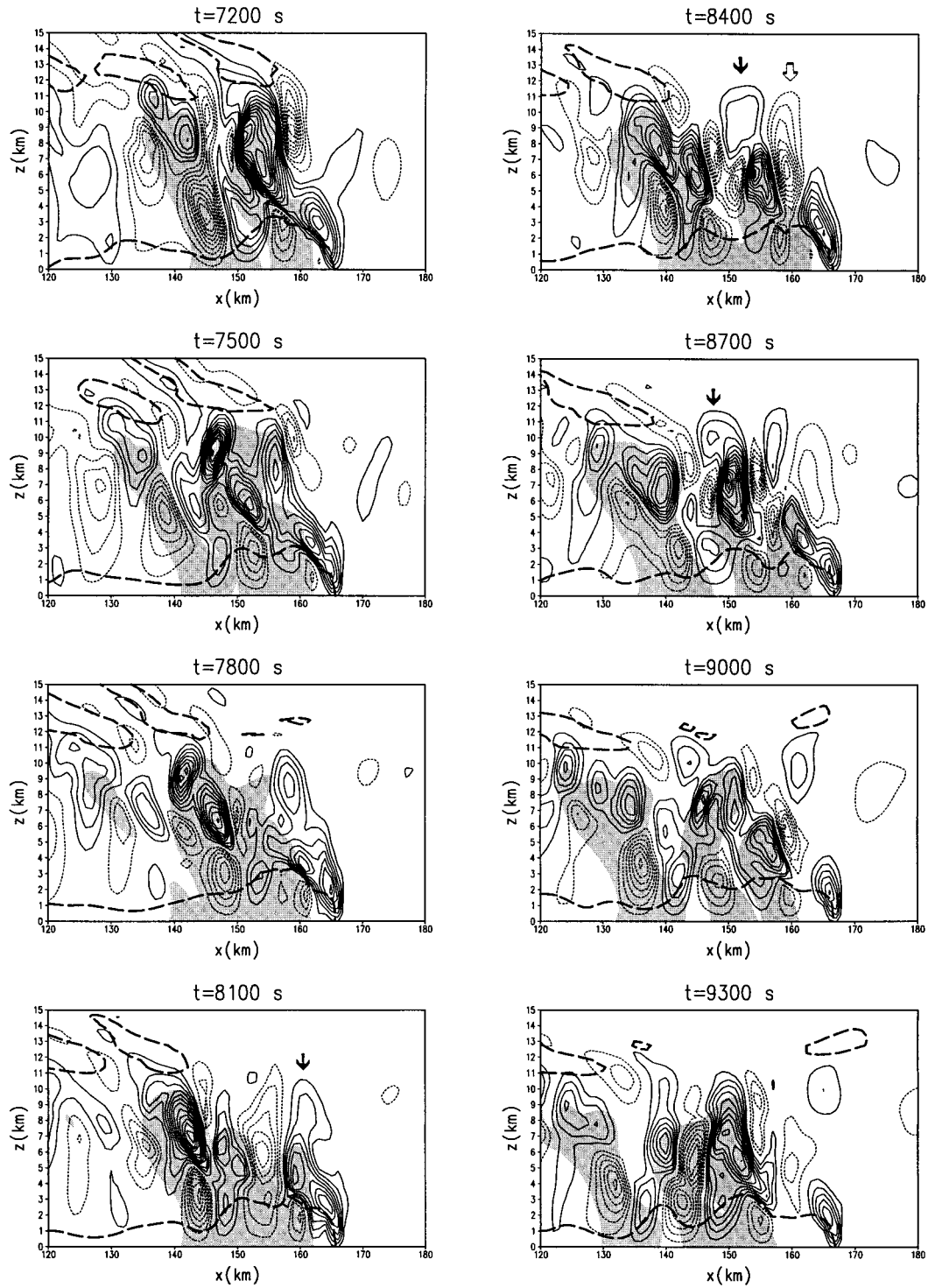


FIG. 10. Vertical profiles of vertical velocity (thin contours in intervals of  $1 \text{ m s}^{-1}$ ) for a portion of the domain in the moving frame of reference with the gust front for the  $\Delta U = 7.5 \text{ m s}^{-1}$  case initialized with the Weisman and Klemm (1982) sounding. The density current is represented by the  $-1\text{-K}$  potential temperature perturbation contour (bold dashed) near the surface. The rainwater is shaded ( $>0.0005 \text{ g kg}^{-1}$ ). The corresponding integration time is shown at the top of each panel.

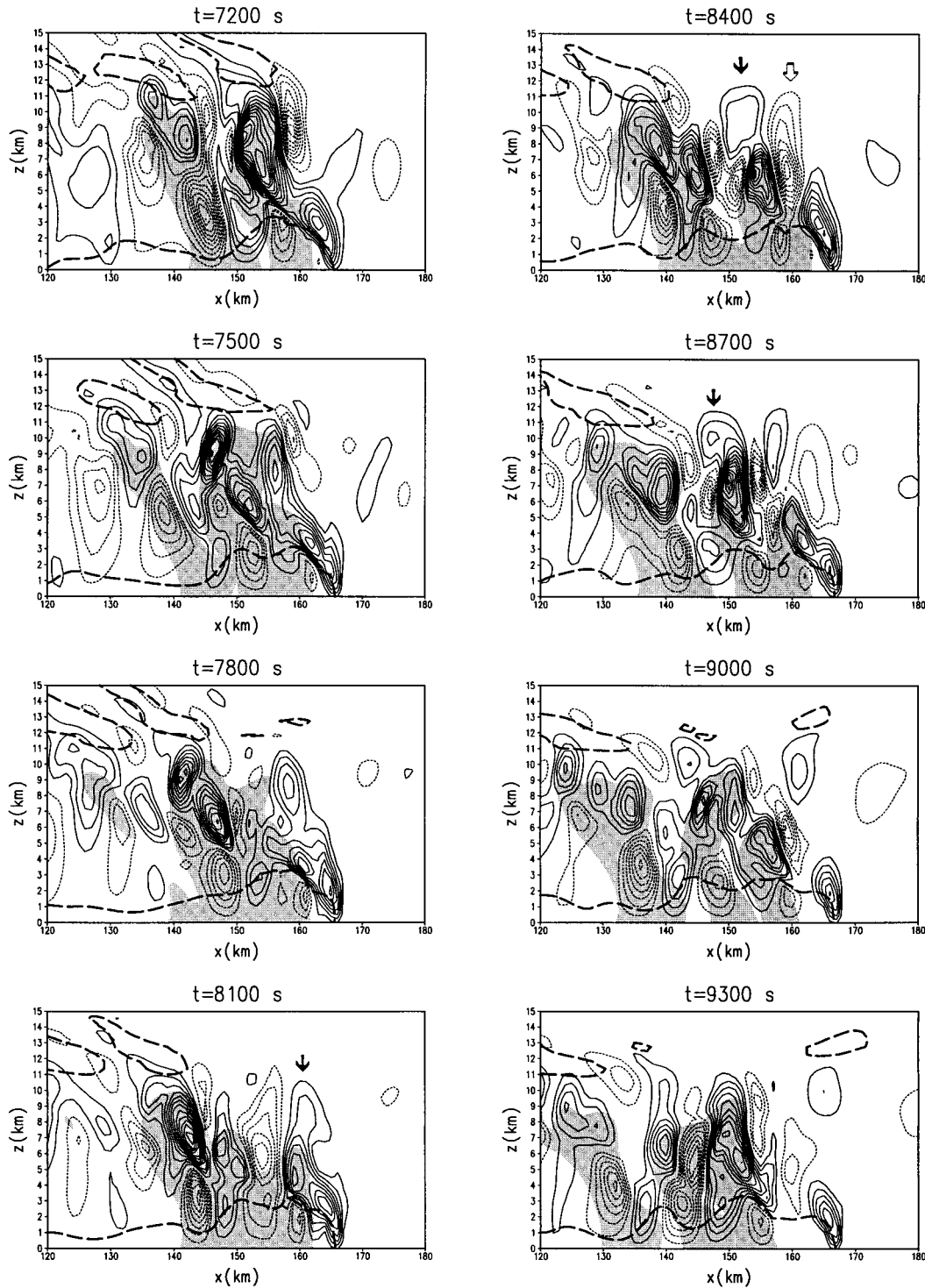


FIG. 10. (Continued)

where  $Q_0$  is the magnitude of diabatic forcing (negative for cooling),  $a_1$  the half-width of the bell-shaped function, and  $d$  is the cooling depth. The second term with  $a_2$  was included to avoid a net forcing problem in an inviscid, steady-state fluid system (Smith and Lin 1982).

An example of this function can be found in Fig. 2 (curve 2) of Smith and Lin. The heat sink half-widths are 15 km ( $a_1$ ) and 150 km ( $a_2$ );  $d = 4$  km in the vertical, its westernmost boundary is located 160 km from the left boundary of the domain, and its lower boundary is

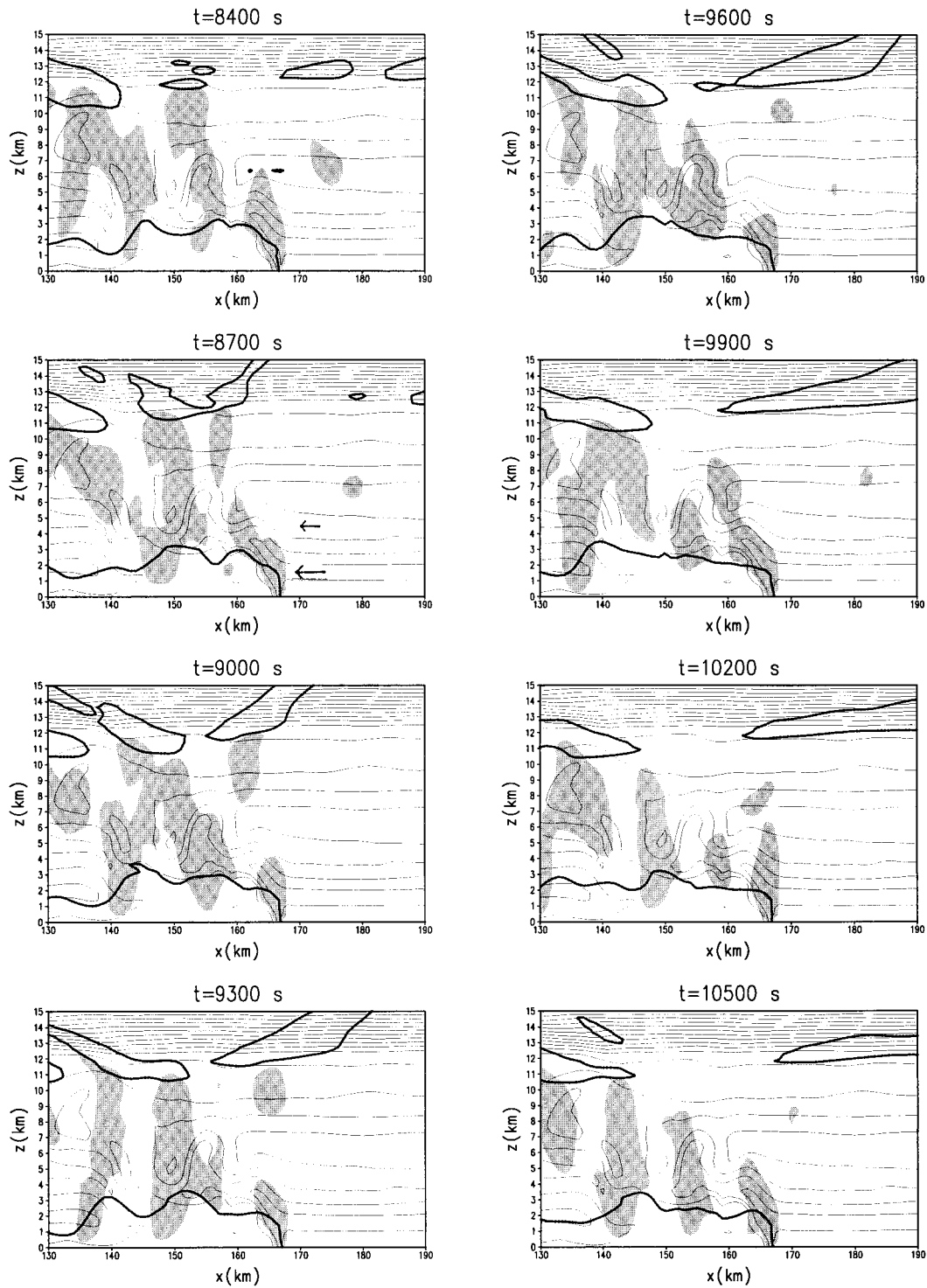


FIG. 11. Vertical cross sections of vertical velocity (shaded for  $w > 1 \text{ m s}^{-1}$ ) and equivalent potential temperature fields for the case of  $\Delta U = 7.5 \text{ m s}^{-1}$  initialized with the Weisman and Klemp (1982) sounding. Only a portion of the computational domain in the moving frame of reference with the gust front is shown. The corresponding time is shown at the top of each panel. The density current is denoted by solid bold curve near the surface.

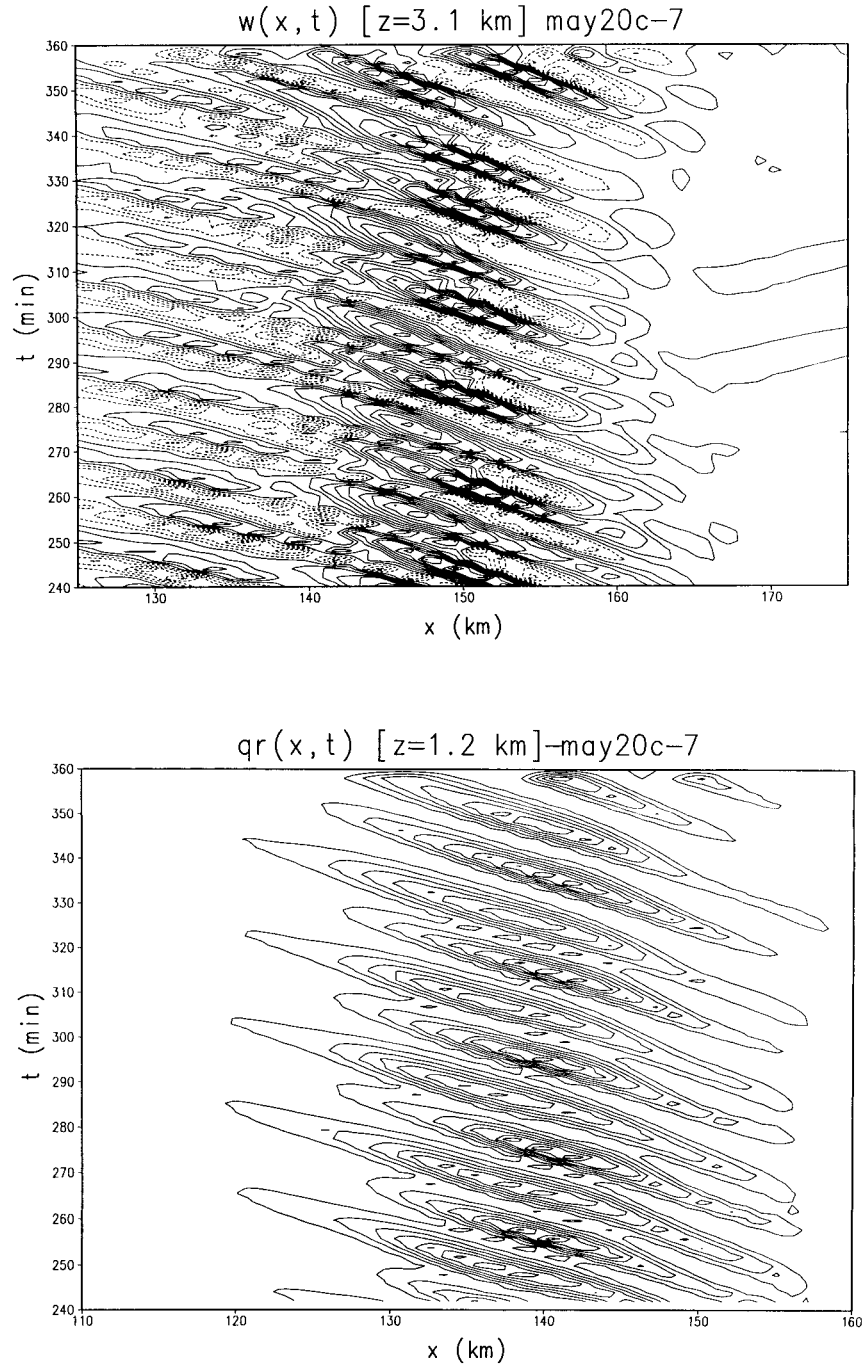


FIG. 12. Time-space plots of vertical velocity at  $z = 3.1$  km for the  $\Delta U = 7.5$  m s $^{-1}$  case initialized with the Weisman and Klemp (1982) sounding.

at the surface. The continuous cooling rate ( $Q_o$ ) of the heat sink is  $-36$  K h $^{-1}$ . This value of  $Q_o$  was modeled after that employed by Jin et al. (1996;  $-34$  K h $^{-1}$ ) to initialize an observed density current within their two-dimensional model.

The cool, dense air from the heat sink was allowed to spread laterally in both right (east) and left (west) directions, no moisture was included for 2 h (7200 s).

The east side of the density current met easterly low-level winds and strong convergence was produced that resulted primarily in a vertically oriented gust front updraft similar to that described previously by Rotunno et al. (1988). The west side of the cool air produced vertical motion that was more slanted because the vorticity produced by both the gust front and the wind shear were positive. The convection that was produced on the west

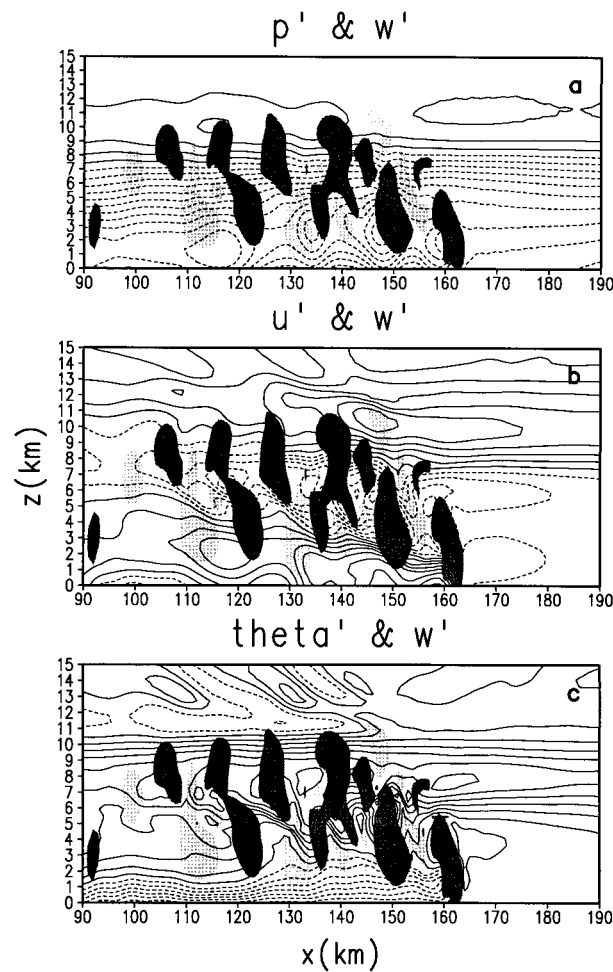


FIG. 13. (a) Perturbation pressure, (b) perturbation horizontal velocity, and (c) perturbation potential temperature contour fields with vertical velocity (dark shaded for  $w > 1 \text{ m s}^{-1}$  and light shaded for  $w < -1 \text{ m s}^{-1}$ ) at  $t = 15\,300 \text{ s}$  for the  $\Delta U = 7.5 \text{ m s}^{-1}$  case initialized with the Weisman and Klemp (1982) sounding.

side of the heat sink after moisture was introduced into the model was short-lived. Therefore, the entire focus of this experiment was the section of the domain to the right of the heat sink.

After 7200 s, moisture was introduced into the model and convective cells began to form above the GFU. The delayed moisture introduction of 2 h was determined in order to give the cool air the opportunity to fully spread away from its parent heat sink into a quasi-steady density current. Therefore, the gust front initiated convection that was not influenced by the heat sink in any way. Rainwater was activated in these experiments, but evaporative cooling was suppressed as in the plateau cases in order to produce a more steady (idealized) cold pool to more clearly study the cell generation and motion. Although downdrafts induced by water loading exist, they do not result in gust front oscillation within any of the heat sink simulations. As in the plateau simulations, the purpose of having a nonoscillating gust front

TABLE 2. Results of idealized sounding multicell simulation.

$\Delta U$ ( $\text{m s}^{-1}$ )	$C_{dc}$ ( $\text{m s}^{-1}$ )	SRMLI ( $\text{m s}^{-1}$ )	Period of cell regeneration (min)
7.5	13.7	-6.2	9.23
10	14.4	-4.4	10.44
15	16.4	-1.4	13.30

serves to either prove or disprove the gust front oscillation mechanism. Since the heat sink was employed throughout the entire simulation, the density current continues to move and gain strength as an actual cold pool would by evaporative cooling from precipitation although in a more steady fashion. Due to the continuation of the fixed heat sink throughout the simulation, the domain was not translated with the moving gust front, but the horizontal domain of 500 km is sufficiently large to contain these storms with no lateral boundary interference.

Four different wind shear profiles were used to initiate the model (see Fig. 15). To test the advection mechanism, four midlevel basic wind profiles were adopted for this series of experiments. The surface velocity of  $-7.5 \text{ m s}^{-1}$  is fixed, which increases to 3, 6, 8.5, and  $12.5 \text{ m s}^{-1}$  at  $z = 2.5 \text{ km}$  ( $\Delta U = 10.5, 13.5, 16,$  and  $20 \text{ m s}^{-1}$ ;  $U_z = 4.2 \times 10^{-3}, 5.4 \times 10^{-3}, 6.4 \times 10^{-3},$  and  $8 \times 10^{-3} \text{ s}^{-1}$ ) and is uniform above this height. For each simulation, the speed of the density current was calculated and its velocity was subtracted from the basic wind in order to discover the midlevel inflow in the frame of reference of the gust front. Based on the results of both the multicell storm and the plateau simulations,

**PERIOD vs. SRMLI: Idealized Sounding Simulations**

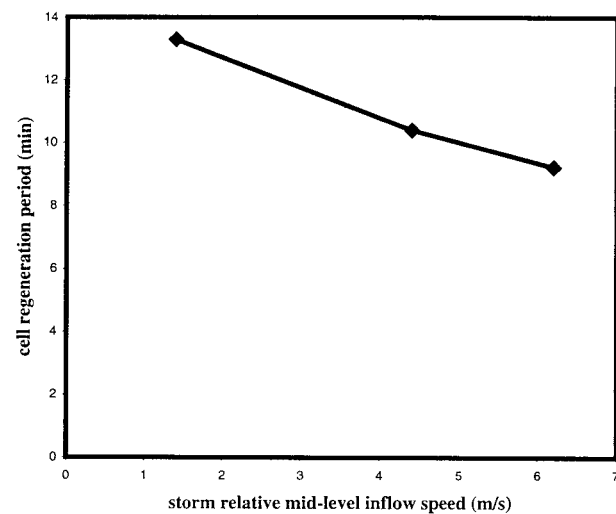


FIG. 14. Cell regeneration period vs the storm-relative midlevel inflow speed for the Weisman and Klemp (1982) sounding initialized simulations.

### Wind Speed Profiles for Heat Sink Simulations

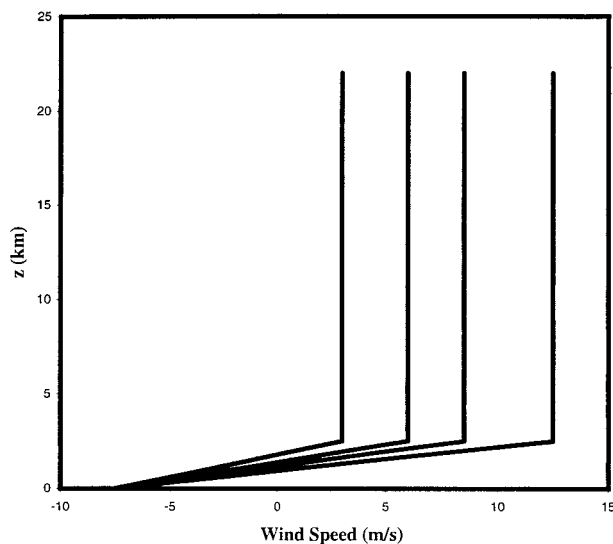


FIG. 15. Basic wind profiles utilized for the initialization of the heat sink multicell simulations.

the cell regeneration period must decrease as the mid-level inflow speed increases if the advection mechanism is a valid explanation for cell regeneration and propagation in a multicell storm with these conditions. Also, if the gust front oscillation mechanism is valid, periodic cell generation will not occur in these simulations that do not allow gust front oscillation.

#### b. Results of heat sink experiments

Prior to  $t = 2$  h (7200 s, not shown), a persistent updraft was found at the eastern edge of the density current (gust front) caused by a strong surface convergence. Weak gravity waves were excited by the GFU but dissipated quickly as they proceeded horizontally and vertically away from the gust front. Following the introduction of moisture into the model at  $t = 2$  h, convective cells were immediately created in association with the strong vertically oriented GFU. By 165 min (9900 s, not shown), the oscillations of the convective pattern above the gust front became generally organized (quasi-steady) in all four shear cases. The period of organization for these heat sink–initialized multicell storms was not as lengthy as those of simulated storms initialized with a thermal bubble due to the fact that the density current that needs to be created by a multicell storm was already in place here. The simulations were carried out through  $t = 6$  h (21 600 s) to capture the most mature stage of the storm.

Figure 16 illustrates the  $w$  contours, cold outflow from the heat sink, and shaded rainwater mixing ratio ( $>0.0005$  g kg $^{-1}$ ) for the largest shear case ( $\Delta U = 20$  m s $^{-1}$ ) from  $t = 12$  300 to 14 400 s in 5-min increments. The heat sink gives rise to an almost uniform cold out-

flow with a constant depth of  $\sim 1.8$  km. However, in the regions of surface precipitation (gray shading) the rainfall causes the current to become shallower due to water loading. Ordinarily, in the real atmosphere, the rainfall would cause an enhanced (deeper) cooling region due to evaporative cooling. Evaporative cooling in these cases was deactivated in the model so the density current is not unduly accelerated. Here, the heat sink was already supported by the continual heat sink to the west and did not need to be sustained by the cooling effects of the rainfall. It should also be noted that unlike the plateau tests, the cold outflow shown has a visible head or nose just behind the gust front indicating the presence of positive horizontal vorticity that serves to oppose the low-level wind shear to create optimal conditions for convection. The vorticity was also seen in vertical cross sections of wind vectors and streamlines (not shown).

For each of the times displayed, a GFU that is in varied stages is observed along the leading edge of the cold pool. For instance, the GFU has grown vertically to  $z = 10$  km along the leading edge of the density current at time  $t = 12$  300 s (see bold arrow). The GFU has produced a cell with updrafts still attached to the GFU that are tilted rearward over the density current head at time  $t = 12$  600 s. At this time, a compensating downdraft (open arrow) to the east of the newly generated cell is in the process of dividing the cell from the gust front. This cell is followed by the bold arrow throughout its lifetime. Each time shown displays four major updrafts or cells (excluding the GFU) in the region from 45 km to the rear of the gust front to the gust front that are in various levels of development. In this case, these individual cells are not advected rearward a great distance behind the GFU. The strong shear of the low-level winds causes the westerly basic wind above  $z = 2.5$  km to be so large (20 m s $^{-1}$ ) that when the speed of the gust front is subtracted, the storm-relative midlevel, front-to-rear inflow is very small, that is, 0.13 m s $^{-1}$  (Table 3). Both cell merging and splitting are detected in this case, which will be investigated closely in section 5.

On the other end of the wind shear spectrum, Fig. 17 illustrates vertical cross sections similar to Fig. 16 except for the  $\Delta U = 10.5$  m s $^{-1}$  case. The differences between this case and that of the  $\Delta U = 20$  m s $^{-1}$  case are evident. First, it is more difficult to see the vertical growth of the GFU and its rearward tilt even though a smaller vertical velocity contour interval (0.75 m s $^{-1}$ ) is utilized. Although the process of GFU growth, tilting, and cell separation still exists in this low-shear simulation, it is not as apparent in this figure with a 5-min time increment because the midlevel inflow is so large ( $-7.139$  m s $^{-1}$ ) that the cells are quickly separated and advected away from the GFU before this process can be seen. For example, at  $t = 14$  400 s, the most recently generated cell is first visible at  $x = 328$  km which is 15 km to the rear of the gust front (at  $x = 343$  km).

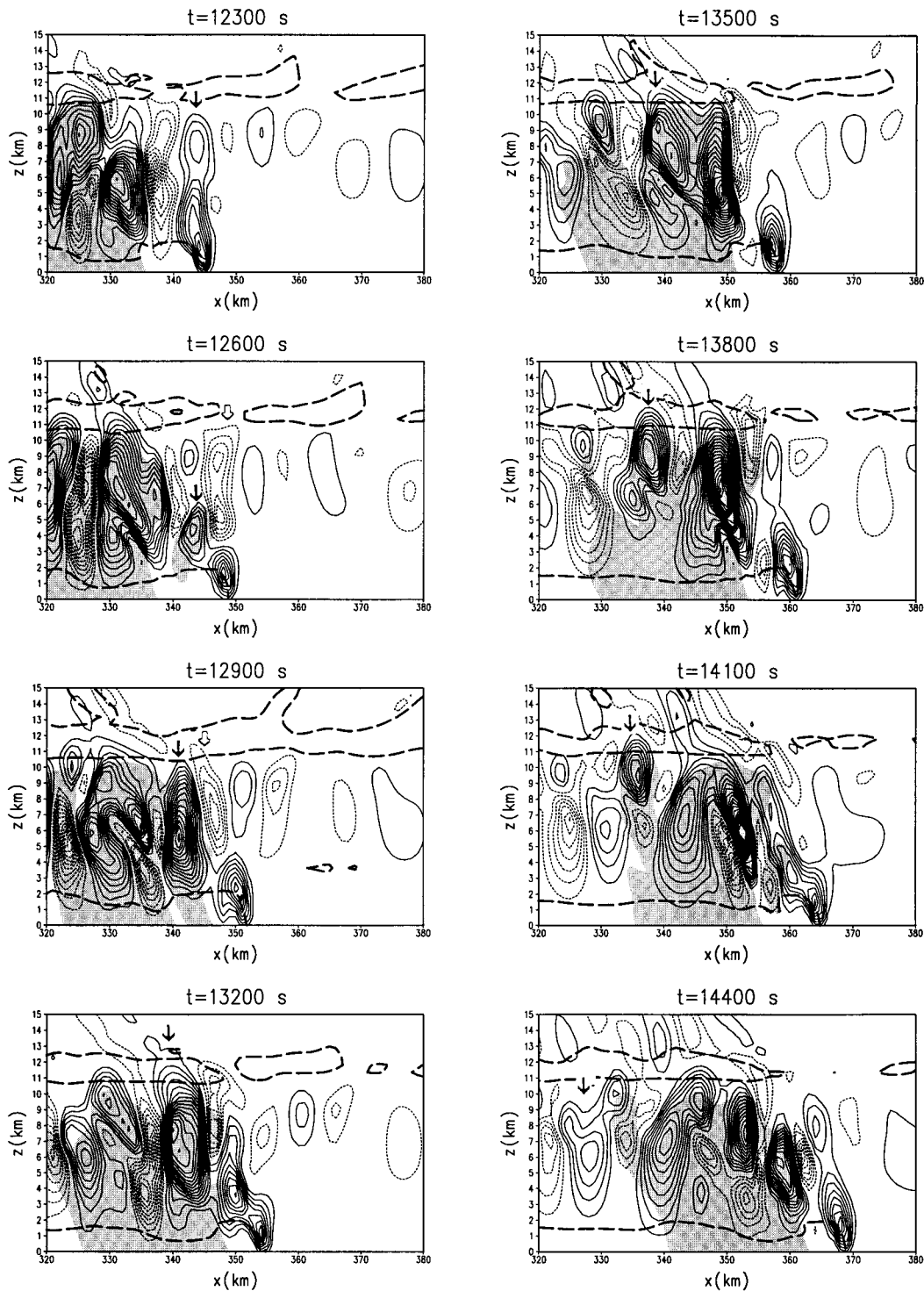


FIG. 16. Same as Fig. 10 except for the heat sink simulation with  $\Delta U = 20 \text{ m s}^{-1}$ .

The cells in this simulation reach their maximum intensity at  $\sim 30 \text{ km}$  behind the gust front as compared to  $15\text{--}20 \text{ km}$  in the  $\Delta U = 20 \text{ m s}^{-1}$  case. Therefore, the cells have a longer growing mode. The convective cells

in this case are more independent of one another and resemble those of a strong evolution multicell storm (Foote and Frank 1983). Although the  $\Delta U = 10.5$  and  $20 \text{ m s}^{-1}$  shear cases produced two rather different types

TABLE 3. Results of heat sink simulation results.

$\Delta U$ ( $\text{m s}^{-1}$ )	$C_{dc}$ ( $\text{m s}^{-1}$ )	Midlevel basic wind speed ( $\text{m s}^{-1}$ )	SRMLI ( $\text{m s}^{-1}$ )	Period of cell regeneration (min)
10.5	10.139	3.0	-7.139	8.00
13.5	10.550	6.0	-4.55	9.23
16	11.389	8.5	-2.889	10.00
20	12.639	12.5	-0.13	15.00

of multicell storms, the same mechanism was responsible for cell regeneration along the gust front and cell propagation.

Time-space plots of  $w'$  for the  $\Delta U = 10$  and  $20 \text{ m s}^{-1}$  cases from 2 h (120 min) to 4 h (240 min) at  $z = 2.7 \text{ km}$  are shown in Figs. 18 and 19. Since the gust front was moving within the domain, these time analyses look different from those in section 3, although the cell movement with time is still clearly illustrated. In Fig. 18, the positive vertical velocity of the GFU begins at  $t = 120 \text{ min}$  at  $x = 270 \text{ km}$  and by  $t = 240 \text{ min}$ , the gust front has propagated to  $x = 344 \text{ km}$ . The difference between the speed of the growing mode and propagating mode is apparently shown by the differing angles of the constant phase lines. Similar features are also shown in Fig. 19. Since the midlevel inflow is weak in this simulation, the gravity waves induced by the top of the strong convection at the GFU are allowed to move eastward.

The cell regeneration periods estimated from these time-space plots of  $w'$  are 8, 9.23, 10, and 15 min for the  $\Delta U = 10.5, 13.5, 16,$  and  $20 \text{ m s}^{-1}$  cases, respectively. The cell regeneration period and SRMLI data for each case is summarized in Table 3. As in LDK and sections 3a and 4c of this study, the cell regeneration period decreases as the storm-relative midlevel inflow increases. The relationship between these two values is displayed in Fig. 20. *Thus, the advection mechanism is supported as one explanation for cell generation, growth, and propagation within these simulated multicell thunderstorms that were initialized with a heat sink.* Since periodic cell generation did occur along the gust front without gust-front oscillation, the gust front oscillation mechanism is not a necessity for cell generation within these simulations.

## 5. Mechanisms of cell splitting and merging

By close examination of all multicell storm-type simulations performed in sections 3–5, two distinct features became evident: convective cell splitting and merging. From analysis of vertical cross sections of  $w'$ , these processes appeared to occur when the cells had begun to propagate rearward over the nose of cold density current air after separating with the GFU and had reached their maximum state of updraft intensity. Although cell splitting and merging were displayed in the simulation figures of several multicell storm studies

(e.g., FO89; Fovell and Dailey 1995; LDK) and certain simulations from earlier sections in this study, little research has been performed to investigate the cause of this cell characteristic.

It has been hypothesized (e.g., Klemp and Wilhelmson 1978; Thorpe and Miller 1978) that precipitation loading from a mature cell as well as evaporative cooling associated with rainwater may cause a downward flux or drag of air within the central cores at low levels, which tends to divide the updraft cell into two distinct updrafts. While this hypothesis is plausible, cell splitting was also apparent in the multicell simulations of LDK where model precipitation was not allowed. Thus, they hypothesized that the cell splitting may be due to the manifestation of gravity waves during the cell propagating mode.

In order to further explore the process of cell splitting and merging behind a gust front, the cell structure of a multicell simulation with precipitation from Fovell and Dailey (1995) was examined since it clearly illustrates cell splitting and merging (although not noted in their discussions). Also, a heat sink–initialized multicell simulation was performed without precipitation, so it could be compared with the results of a simulation in section 4, which revealed cell splitting, merging, and included precipitation.

### a. Fovell and Dailey simulation

Fovell and Dailey (1995) performed many two-dimensional multicell simulations that tested varying shear depth profiles. Figure 21 (their Fig. 9) shows vertical cross sections of  $w'$  through the gust front from their simulation with a shear layer depth  $D$  of 5 km. This simulation by Fovell and Dailey (1995) is said to be complex periodic, that is, when “two or more cells are produced within a certain time period, which represents the shortest period over which the storm has a sufficient degree of periodicity.” Five (not equally spaced) times during the simulation are shown. Though Fovell and Dailey (1995) did not remark about these features, cell splitting and merging are visibly evident in this figure.

In Fig. 21a, a cell (labeled m1) has just been generated at the gust front (or what they label as FL—forced lifting area). By the second panel  $t + 6$  (Fig. 21b), m1 has separated from the GFU, has moved rearward, and has begun to split into m1 and m1\*. Meanwhile, another cell, M1 is forming at the gust front. Figure 21c shows that M1 is tilted to the rear, has grown, but is still connected to the GFU. Cells m1 and m1\* have become completely independent at this time ( $t + 12$ ). Eight minutes later, in Fig. 21d ( $t + 20$ ), M1 has also begun to split into cells M1 and M1\*. Cell m1 (shown with an italicized cell label that is an addition to Fovell and Dailey’s original analysis), however, has not moved rearward and has partially combined with M1\*. Cell m1\* (also in italics) has merged with a previously gen-

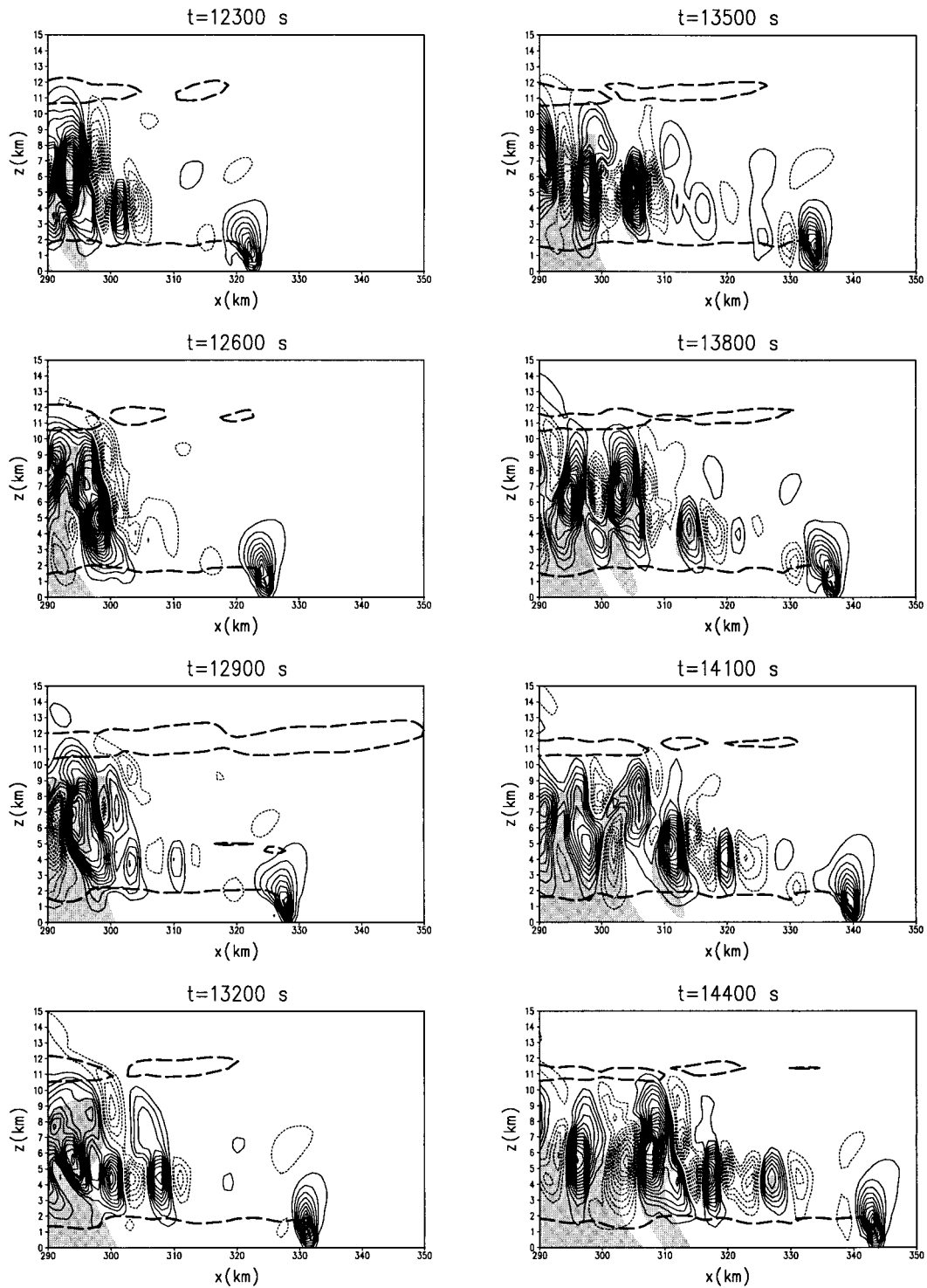


FIG. 17. Same as Fig. 10 except for the heat sink simulation with  $\Delta U = 10.5 \text{ m s}^{-1}$  and a vertical velocity contour interval of  $0.75 \text{ m s}^{-1}$ .

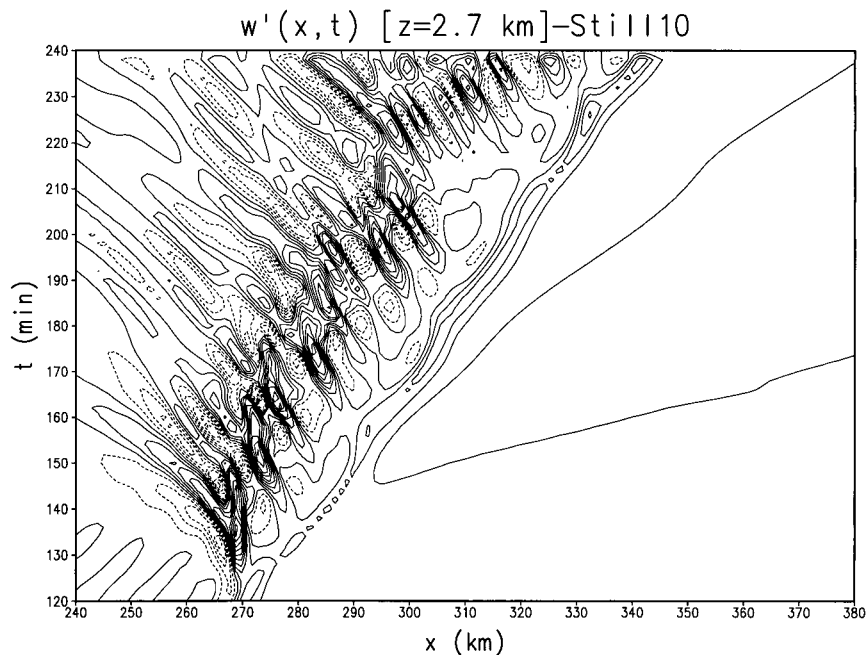


FIG. 18. Time-space plots of vertical velocity at  $z = 2.7$  km is given for the heat sink multicell simulation with  $\Delta U = 10.5$  m s $^{-1}$ . Contour interval is 1 m s $^{-1}$ . Positive (negative) values are solid (dashed).

erated cell M0\* at  $x = 35$  km. Figure 21e shows the joined cells of (M0\* + m1\*) and (m1 + M1\*) continuing to move rearward over the cold outflow current together while another cell, m2, is created along the gust front that is beginning to merge with the remnants of M1. This simulation is an excellent example of cell splitting. The division of the cells by the downward motion occurred in each case when the cell updraft had reached its highest magnitude.

#### b. Simulation with heat sink and rainwater

Before inspecting the nonprecipitating simulation, a more concentrated examination of an example of cell splitting and merging from the heat sink initialized multicell simulation with  $\Delta U = 20$  m s $^{-1}$  which includes precipitation (from section 4) is needed for comparison. Figure 22 shows a closer view of  $w'$  over the cold density current of this simulated storm from  $t = 10\,800$  s (180 min) to  $t = 12\,300$  s (205 min) in 5-min increments. As in previous figures, positive rainwater mixing ratio is shaded. At  $t = 10\,800$  s, the GFU is shown at the leading edge of the cold pool. Just behind the gust front, the convective cell C1 has been tilted rearward and is just beginning to separate from the GFU. The most mature and strongest cell shown at this time is cell C0. Cell C0 has begun to produce surface precipitation and is beginning to divide into C0 and C0\* below  $z = 7$  km because of the negative vertical velocity seen here. By  $t = 11\,100$  s, the GFU has expanded vertically as it begins to tilt and produce another cell. The mature cell C0 has now

completely separated into two distinct cells: C0 and C0\*. Cell C1 is independent of the GFU and has now partially merged with the split cell C0\*. The next time, 11 400 s, shows that cells (C1 + C0\*) have completely merged into one cell but by  $t = 11\,700$  s, (C1 + C0\*) is separated by downward motion at  $x = 322$  km and are two totally distinct cells again by 12 000 s.

It was revealed from the analysis of the cells in this simulation that once a cell reaches its maximum strength and begins to produce precipitation, it will be split by the water-loaded downdraft that develops within the updraft core. After this split, the western (left) cell continues to dissipate and progress rearward. Here, the forward split cell tends to merge with a newly generated GFU cell. Because of the high shear in this case, the midlevel inflow is not large ( $\sim 0.13$  m s $^{-1}$ , see Fig. 15), consequently, the cells are not advected quickly away from the GFU and are inclined to merge together. This is not the case for all multicell storms, only those that have a weak front-to-rear midlevel flow speed. Splitting, however, is observed in most simulated multicell storms with a wide range of shear values. For example, all of the four heat sink-initialized storms presented in section 4 contain cell splitting features. The growing mode and propagating mode are easily seen in this simulation. The generated cells continue to grow until their maximum intensity is reached at  $\sim 15$  km behind the gust front.

#### c. Simulation with heat sink and no rainwater

The same simulation as described just above was performed with no rainwater included in the model cal-

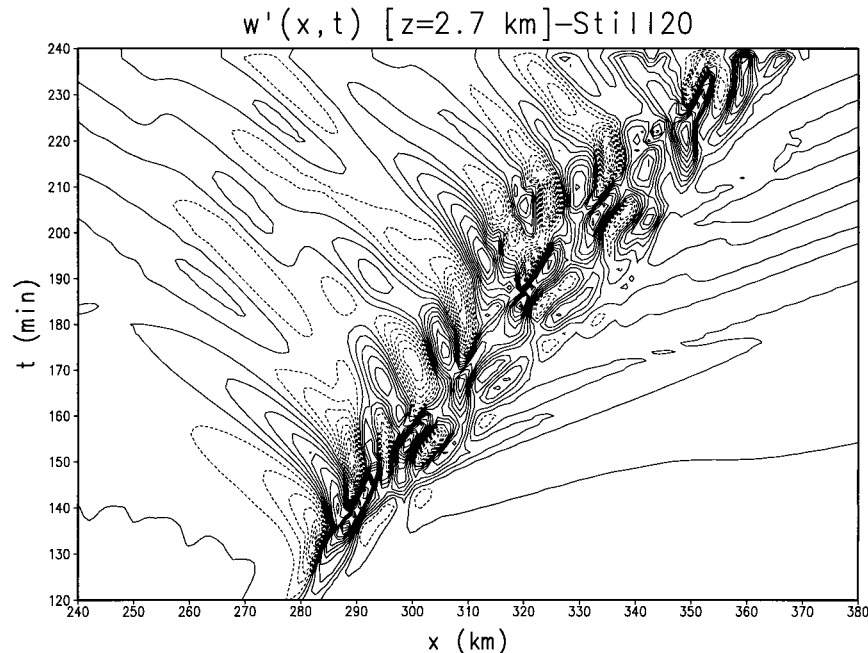


FIG. 19. Same as Fig. 18 except for the  $\Delta U = 20 \text{ m s}^{-1}$  case.

culations. The results from this case (Fig. 23) are somewhat different from that with rainwater (Fig. 22) because, although splitting is shown, it did not occur as frequently. At  $t = 10\,800$  s, one major convective cell, C1, is shown. Although there can be no rainwater drag or evaporative cooling, a weak downdraft is shown that seems to be dividing C1. By  $t = 11\,000$  s, this cell has completely split into C1 and C1\*. At  $t = 11\,400$  s, a

new cell, C2, is generated along the gust front and C1\* is beginning to split below 3 km. By  $t = 11\,700$  s, C1\* has split into C1\* and C1\*\*. Five minutes later,  $t = 12\,000$  s, C1\*\* has merged with cell C2 (C1\*\* + C2). In addition, the cell tilting/compensating downdraft cutoff cycle and periodic cell regeneration are still apparent within Fig. 23 even without the effects of water loading associated with rainwater. This simulation demonstrates that within the heat sink simulations, water loading induced downdrafts (which may cause gust front oscillation) are not required for periodic cell formation along the gust front.

#### PERIOD vs SRMLI: Heat Sink Simulations

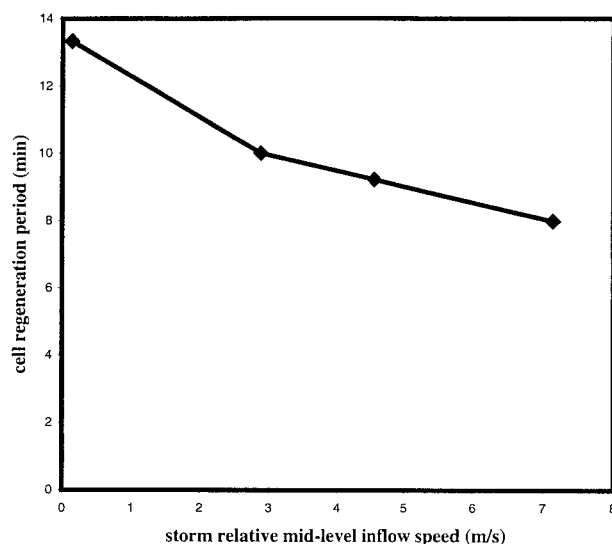


FIG. 20. Cell regeneration period vs the storm-relative midlevel inflow speed for the heat sink–initialized multicell simulations.

The merging of cells was found to be dependent on the rearward speed of cell propagation. If the storm-relative midlevel inflow is weak (e.g., Figs. 22 and 23), then the cells move rearward more slowly and tend to merge together. In the cases within this study where the midlevel inflow is high (e.g., Fig. 17), cell merging was not seen as frequently. However, from the previous cell splitting analysis, cell merging normally occurs between a newly generated cell and the right (east) member of a mature split cell. The right member of the divided cell continues to intensify (remains in the growing mode) after its separation and does not propagate rearward as quickly as its left counterpart, which has entered the propagation mode. Because of its slow movement, the right mature cell unites with the most recently produced cell. Therefore, cell splitting induces cell merging.

Cell splitting does occur within multicell storm simulation without precipitation, although it does not occur as frequent as cases with precipitation. Therefore, some factor other than precipitation loading and cooling must

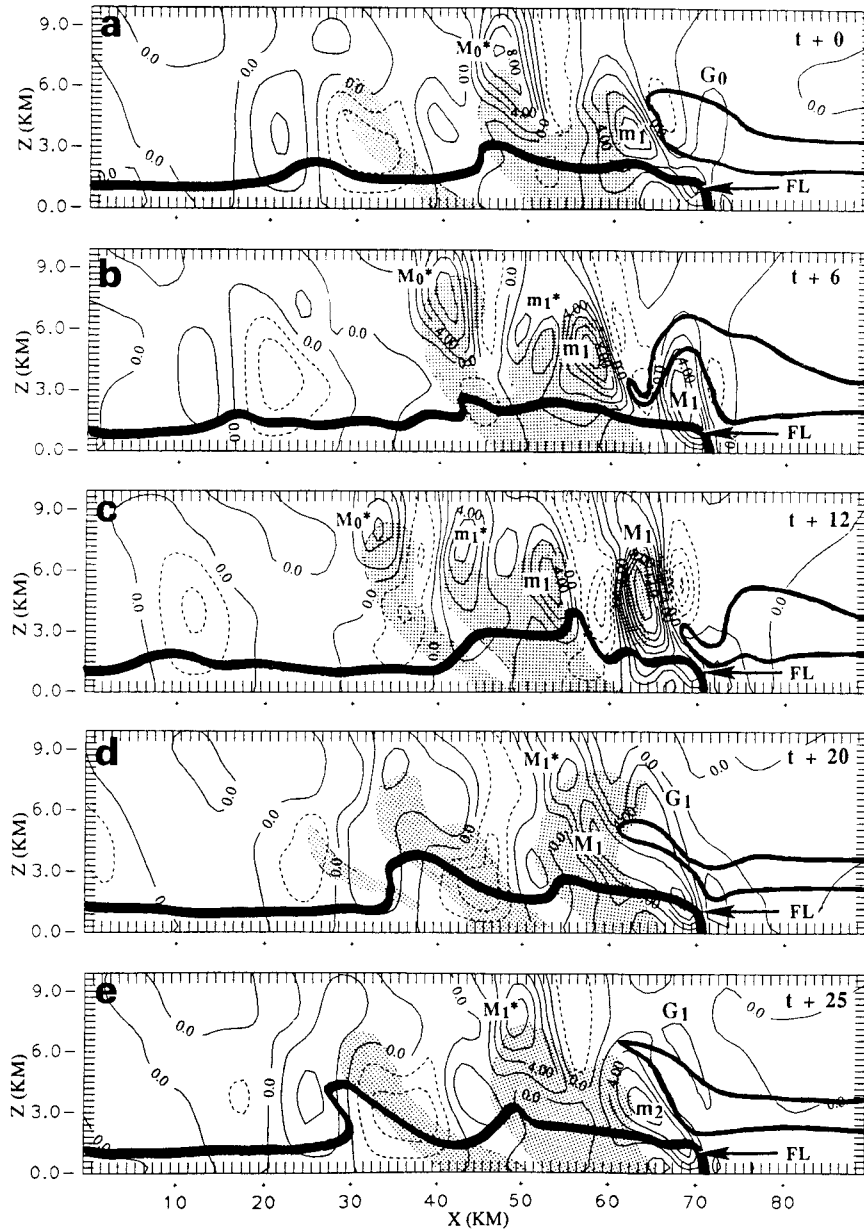


FIG. 21. Vertical profiles of vertical velocity contours with rainwater shading from Fovell and Dailey (1995). The density current is depicted with the  $-1\text{-K}$  perturbation temperature contour (bold solid line). The gust front (FL), major cells (M), minor cells (m), and gravity wavelike disturbances (G) are labeled. Additional analysis was made to the original Fovell and Dailey (1995) figure by this study. The additions are labeled with letters (M, m).

be responsible for the initiation of cell splitting. Cell division was shown to begin in the low levels ( $z < 4$  km) of the cell and with time, the entire depth of the cell was separated. Before reaching its maximum intensity (in the growing mode), the lower portion of a convective cell was tilted westward (seen in Fig. 23,  $t = 12\,000$  s,  $x = 334$  km). As the cell reaches its most intense state, the west side of the cell became more vertical in low levels while the east side remained tilted. Thus, the lower part of the cell began to split. The initial

separation occurred at low levels first because the gust front relative low-level inflow is stronger than that in the middle levels. This differential advection caused the lower, western portion of the cell to become more vertically oriented. A forward compensating downdraft for the west side (vertical part) of the cell then formed and continued to completely split the cell throughout its upper levels. Thus, we hypothesize that the *vertical differential advection mechanism is responsible for cell splitting*.

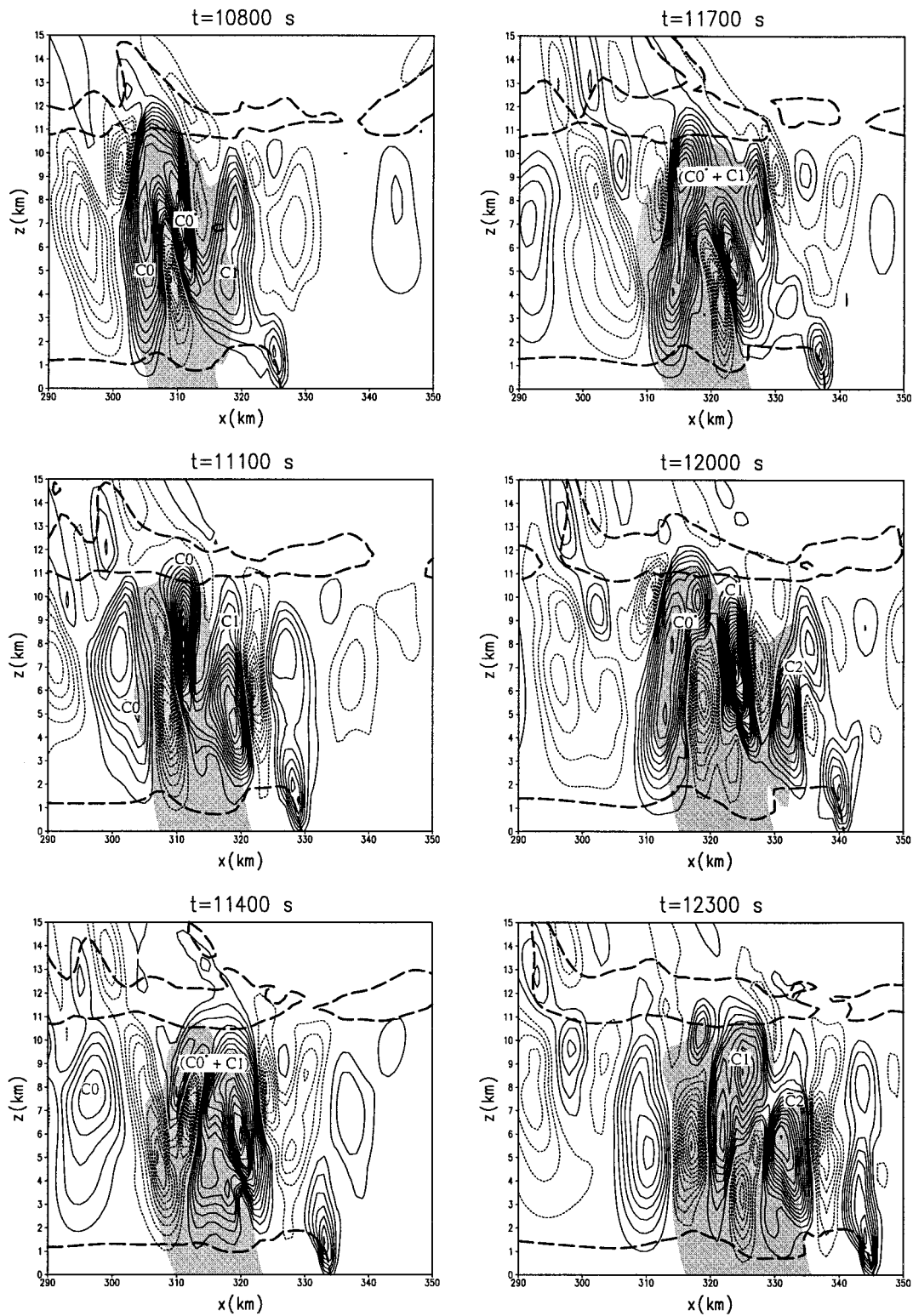


FIG. 22. Same as Fig. 10 except for the  $\Delta U = 20 \text{ m s}^{-1}$  heat sink–initialized multicell simulation with precipitation loading but no evaporative cooling. A smaller portion of the horizontal domain is shown to focus on cell splitting.

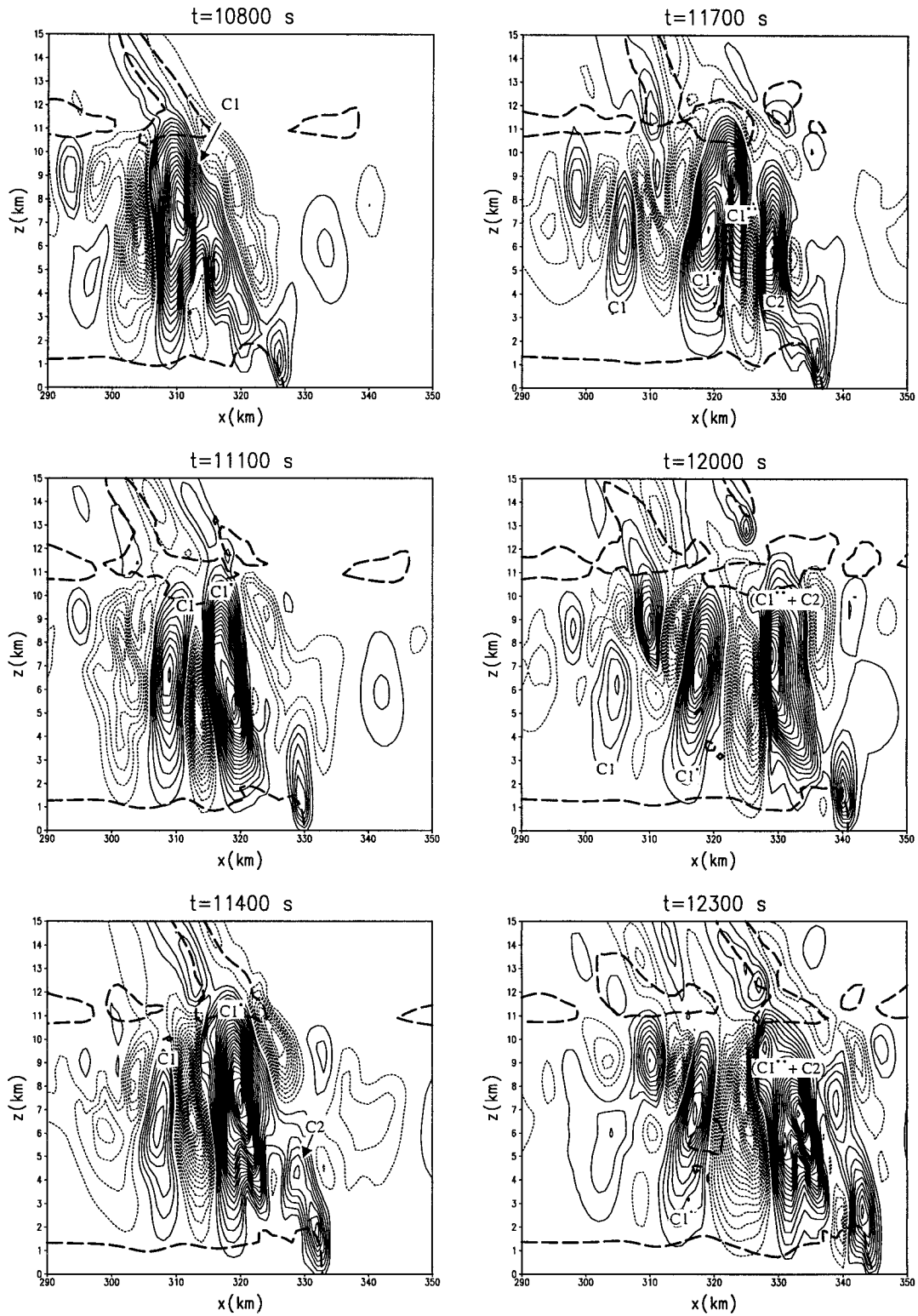


FIG. 23. Same as Fig. 22 except without precipitation.

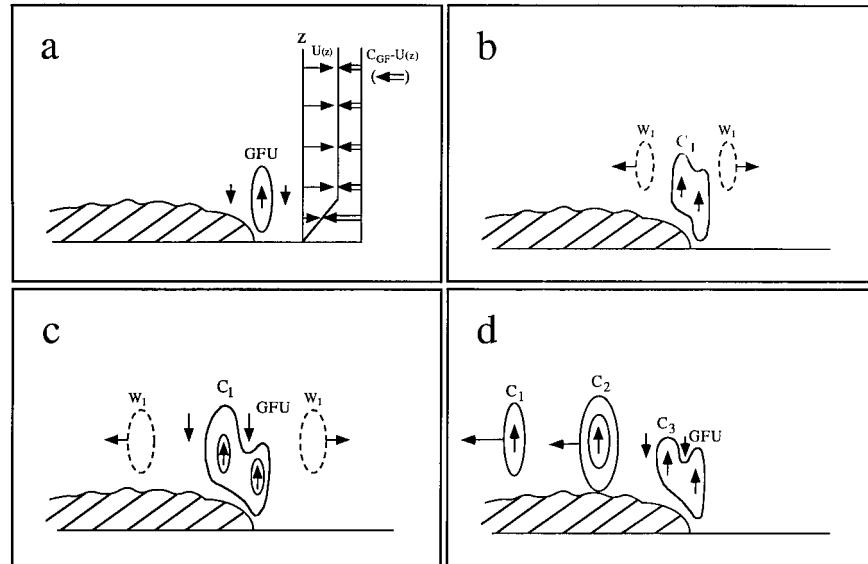


FIG. 24. A schematic model for the cell regeneration and propagation within a 2D multicell thunderstorm. Four stages are found. (a) The formation of the GFU from convergence at the gust front. The convergence is due to the gust front–relative midlevel inflow [subtract gust front speed from basic wind:  $U(z) - C_{GF}$ ]. Compensating downdrafts of the GFU are also shown. (b) Rearward advection of the growing gust front updraft ( $C_1$ ). (c) Cutting off of the growing cell ( $C_1$ ) from the gust front updraft by the upstream compensating downdraft. (d) Cell regeneration ( $C_3$ ) and rearward movement ( $C_1$  and  $C_2$ ).  $C_2$  is at the end of the growing mode (maximum vertical velocity) and  $C_1$  is moving more quickly within the propagating mode. (From Lin et al. 1998.)

It appears that the vertical differential advection mechanism may serve to initially force the splitting of convective cells behind the gust front. The cell splitting process is strongly enhanced by precipitation drag and cooling, and therefore, cell splitting is more frequent and easily seen in modeling cases that include precipitation. However, while precipitation does strengthen cell spitting, this study suggests that it is not necessary to cause cell splitting within a multicell storm.

## 6. Conclusions and discussion

The primary focus of this study was to address some concerns of the *advection mechanism* (Fig. 24) first proposed by LDK and also to use this analysis to reexamine other proposed mechanisms for cell regeneration. A series of carefully designed sensitivity tests were done to test the forcing mechanisms. An analysis of multicell storm splitting and merging was also achieved.

Simulations were designed to investigate the sensitivity of the cell generation, development, and propagation to a rigid lid upper boundary condition, which is occasionally used by some researchers. It was concluded that a rigid lid placed at the top of the domain interfered with the simulation by unnaturally strengthening the development of older cells, lengthening the cell-growing mode, and generating more cells during a fixed time period. Therefore, a rigid lid is not an appropriate upper boundary condition for multicell storm simulations.

Similar to LDK, a plateau was employed to replace the cold outflow from a multicell storm. However, five basic wind profiles, which span a much wider range of low-level shear than that of LDK, were used. Three simulations were performed using an idealized sounding to investigate whether the advection mechanism proposed by LDK works for their particular environment (sounding). A final series of four simulations contained a localized heat sink that spread laterally into a quasi-steady cold outflow similar to that produced by a thunderstorm. This experiment was used to make the density current steady in order to isolate the process of cell regeneration from other disturbances. Unlike the plateau, however, the heat sink provided a more realistic density current with which mixing could occur and where baroclinically generated vorticity was found in the head. After the cold pool had moved a sufficient distance from the sink, moisture was added to the model, and convective cells were created along the edge of the dense, cold air.

Although varying types of model techniques were used for each of the different sensitivity tests, many similarities were found within their results. First, convergence occurred at the edge of the cold outflow (or plateau), which is responsible for the formation of the gust front updraft (GFU). From midlevel front-to-rear inflow into the storm, the upper portion of the GFU grew vertically into a new convective cell and tilted rearward over the cold dome of the density current. Compensating downdrafts were observed on each side

of the new cell and the right (forward) downdraft divided the growing cell from the GFU. After separation from the GFU, the newly generated cell propagated rearward, advected by the midlevel inflow, and continued to grow (growing mode). At a certain distance behind the gust front, the cell generated its maximum vertical velocity and began to produce falling precipitation. Each sensitivity test performed provided the same result: the cell regeneration period decreases as the storm-relative midlevel inflow (SRMLI) increases. In other words, the stronger the SRMLI, the more cells are generated by the GFU within a certain time span. After this stage (growing mode), the cell continued to move rearward at a faster speed (propagation mode), unloaded the remainder of its rainwater, and began to weaken. The mature cell did not continue its growth because its thermal and moisture support was cut off by the new cell at the GFU. The propagation mode behaves like gravity waves, as described in LDK and YH. Convective cell splitting and merging were observed at the end of the growing mode of an individual cell throughout all the multicell storm simulations in this study. The mature cell often splits into two different cells at that time. If the magnitude of the midlevel inflow was small enough, the right cell of the division tended to merge with the new cell. The storm without precipitation did exhibit cell splitting and merging. It was hypothesized that *vertical differential advection* is responsible for cell splitting in our multicell storm simulation with no precipitation. It appeared, however, that precipitation does serve to enhance the frequency of cell splitting within these simulations. A tilting cell/compensating downdraft hypothesis was developed that appears to be able to explain the cell splitting seen in the multicell simulations of this study. However, a further study is needed to rigorously prove this hypothesis.

The results of the simulations from this study were also used to assess the conclusions from some previous numerical modeling research. A finding from the multicell simulations of FO89 was corroborated with the results of this study. As the low-level shear magnitude (in this study; LDK; and FO89) was increased then the cells produced along the gust front are less discrete or independent of one another. Also, since the steady gust front of both the plateau and heat sink simulations produced periodic cell generation and rearward movement, the gust front oscillation mechanism was found to be unnecessary for cell generation within the simulations of this study.

Although the mechanisms of cell regeneration along the gust front were thoroughly investigated with analysis of the simulations from this project, additional examination of certain areas is needed. Since it was found that gravity waves might control the propagation mode, further research needs to be performed to discover the maintenance of these gravity waves during the propagation mode. Full ice microphysics was used in all the simulations of this study. With the same sounding (from

Fovell and Ogura 1988), similar simulations by Fovell and Ogura (1989) done without ice microphysics resulted in slower gust front speeds. Due to the fact that simulations performed with full ice microphysics result in deeper, denser density currents (LDK), this contrast in gust-front speed may be accounted for. However, carefully designed sensitivity tests for 2D multicell storm simulations would be useful to determine exactly what role microphysics play in cell regeneration along the gust front.

*Acknowledgments.* The authors would like to thank Drs. S. E. Koch, and A. J. Riordan at North Carolina State University and Dr. R. P. Weglarz at Western Connecticut State University for their helpful suggestions and input on this study. Dr. Chang-Min Chu's assistance with the ARPS model, and Dave DeCroix's help on answering computer and modeling questions are also appreciated. The permission from Drs. K. K. Droegemeier and M. Xue for using the ARPS is highly appreciated. This work has been partially supported by NSF Grants ATM-9224595 and ATM-0096876. Part of the computation was performed on the North Carolina Supercomputer Center's workstation cluster.

#### REFERENCES

- Chalon, J.-P., J. C. Fankhauser, and P. J. Eccles, 1976: Structure of an evolving hailstorm. Part I: General characteristics and cellular structure. *Mon. Wea. Rev.*, **104**, 564–575.
- Dudhia, J., M. W. Moncrieff, and D. W. K. So, 1987: The two-dimensional dynamics of West African squall lines. *Quart. J. Roy. Meteor. Soc.*, **113**, 121–146.
- Foote, G. B., and H. W. Frank, 1983: Case study of a hailstorm in Colorado. Part III: Airflow from triple-Doppler measurements. *J. Atmos. Sci.*, **40**, 686–707.
- Fovell, R. G., and Y. Ogura, 1988: Numerical simulation of a mid-latitude squall line in two dimensions. *J. Atmos. Sci.*, **45**, 3846–3879.
- , and —, 1989: Effect of vertical wind shear on numerically simulated multicell storm structure. *J. Atmos. Sci.*, **46**, 3144–3176.
- , and P. S. Dailey, 1995: The temporal behavior of numerically simulated multicell-type storms. Part I: Modes of behavior. *J. Atmos. Sci.*, **52**, 2073–2095.
- , and P.-H. Tan, 1996: Why multicell storms oscillate. Preprints, *18th Conf. on Severe Local Storms*, San Francisco, CA, Amer. Meteor. Soc., 186–189.
- , and —, 1998: The temporal behavior of numerically simulated multicell-type storms. Part II: The convective cell life cycle and cell regeneration. *Mon. Wea. Rev.*, **126**, 551–577.
- Jin, Y., S. E. Koch, Y.-L. Lin, F. M. Ralph, and C. Chen, 1996: Numerical simulations of an observed gravity current and gravity waves in an environment characterized by complex stratification and shear. *J. Atmos. Sci.*, **53**, 3570–3588.
- Klemp, J. B., and D. K. Lilly, 1978: Numerical simulation of hydrostatic mountain waves. *J. Atmos. Sci.*, **35**, 78–107.
- , and R. B. Wilhelmson, 1978: The simulation of three-dimensional convective storm dynamics. *J. Atmos. Sci.*, **35**, 1070–1096.
- Lin, Y.-L., and H.-Y. Chun, 1991: Effects of diabatic cooling in a shear flow with a critical level. *J. Atmos. Sci.*, **48**, 2476–2491.
- , T.-A. Wang, and R. P. Weglarz, 1993: Interactions between gravity waves and cold air outflows in a stably stratified uniform flow. *J. Atmos. Sci.*, **50**, 3790–3816.

- , R. L. Deal, and M. S. Kulie, 1998: Mechanisms of cell regeneration, development, and propagation within a two-dimensional multicell storm. *J. Atmos. Sci.*, **55**, 1867–1886.
- Ogura, Y., and M.-T. Liou, 1980: The structure of a midlatitude squall line: A case study. *J. Atmos. Sci.*, **37**, 553–567.
- Pielke, R. A., 1984: *Mesoscale Meteorological Modeling*. Academic Press, 611 pp.
- Rotunno, R., J. B. Klemp, and M. L. Weisman, 1988: A theory for strong, long-lived squall lines. *J. Atmos. Sci.*, **45**, 463–485.
- Smith, R. B., and Y.-L. Lin, 1982: The addition of heat to a stratified airstream with application to the dynamics of orographic rain. *Quart. J. Roy. Meteor. Soc.*, **108**, 353–378.
- Thorpe, A. J., and M. J. Miller, 1978: Numerical simulations showing the role of the downdraft in cumulonimbus motion and splitting. *Quart. J. Roy. Meteor. Soc.*, **104**, 873–893.
- , —, and M. W. Moncrief, 1982: Two-dimensional convection in non-constant shear: A model of mid-latitude squall lines. *Quart. J. Roy. Meteor. Soc.*, **108**, 739–762.
- Weisman, M. L., and J. B. Klemp, 1982: The dependence of numerically simulated convective storms on vertical wind shear and buoyancy. *Mon. Wea. Rev.*, **110**, 504–520.
- Xue, M., K. K. Droegemeier, and V. Wong, 2000: The Advanced Regional Prediction System (ARPS)—A multi-scale nonhydrostatic atmospheric simulation and prediction model. Part I: Model dynamics and verification. *Meteor. Atmos. Phys.*, **75**, 161–193.
- and Coauthors, 2001: The Advanced Regional Prediction System (ARPS)—A multi-scale nonhydrostatic atmospheric simulation and prediction model. Part II: Model physics and applications. *Meteor. Atmos. Phys.*, **76**, 143–165.
- Yang, M.-J., and R. A. Houze Jr., 1995: Multicell squall line structure as a manifestation of vertically trapped gravity waves. *Mon. Wea. Rev.*, **123**, 641–660.